Atmos. Meas. Tech. Discuss., 4, 7035–7108, 2011
www.atmos-meas-tech-discuss.net/4/7035/2011/
doi:10.5194/amtd-4-7035-2011

Atmospheric Measurement Techniques Discussions

MIPAS-STR measurements in the arctic UTLS in winter/spring 2010: instrument characterization, retrieval and validation

W. Woiwode[1], H. Oelhaf[1], T. Gulde[1], C. Piesch[1], G. Maucher[1], A. Ebersoldt[2], C. Keim[1,*], M. Höpfner[1], S. Khaykin[3], F. Ravegnani[4], A. E. Ulanovsky[3], C. M. Volk[5], E. Hösen[5], A. Dörnbrack[6], J. Ungermann[7], C. Kalicinsky[5], and J. Orphal[1]

[1]Institute for Meteorology and Climate Research, Karlsruhe Institute of Technology, Karlsruhe, Germany
[2]Institute for Data Processing and Electronics, Karlsruhe Institute of Technology, Karlsruhe, Germany
[3]Central Aerological Observatory, Dolgoprudny, Moscow region, Russia
[4]Institute of Atmospheric Sciences and Climate, CNR-ISAC, Bologna, Italy
[5]Department of Physics, University of Wuppertal, Wuppertal, Germany
[6]DLR, Institut für Physik der Atmosphäre, 82230 Oberpfaffenhofen, Germany

[7]Institute of Energy and Climate Research, Research Centre Jülich GmbH, Jülich, Germany
[*]now at: Astrium GmbH, Friedrichshafen, Germany

Received: 7 November 2011 – Accepted: 9 November 2011 – Published: 24 November 2011

Correspondence to: W. Woiwode (wolfgang.woiwode@kit.edu)

Published by Copernicus Publications on behalf of the European Geosciences Union.

Abstract

The mid-infrared FTIR-limb-sounder Michelson Interferometer for Passive Atmospheric Sounding – STRatospheric aircraft (MIPAS-STR) was deployed onboard the stratospheric aircraft M55 Geophysica during the RECONCILE campaign in the arctic winter/spring 2010. From the MIPAS-STR measurements, vertical profiles and 2-dimensional vertical cross-sections of temperature and trace gases are retrieved. Detailed mesoscale structures of polar vortex air, extra vortex air and vortex filaments are identified in the results at a typical vertical resolution of 1 to 2 km and typical horizontal sampling density of 45 or 25 km, depending on the sampling programme. Results are shown for the RECONCILE flight 11 on 2 March 2010 and are validated with collocated in-situ measurements of temperature, O_3, CFC-11, CFC-12 and H_2O. Exceptional agreement is found for the in-situ comparisons of temperature and O_3, with mean differences (vertical profile/along flight track) of 0.2/−0.2 K for temperature and −0.01/0.05 ppmv for O_3 and corresponding sample standard deviations of the mean differences of 0.7/0.6 K and 0.1/0.3 ppmv. The comparison of the retrieved vertical cross-sections of HNO_3 from MIPAS-STR and the infrared limb-sounder Cryogenic Infrared Spectrometers and Telescopes for the Atmosphere – New Frontiers (CRISTA-NF) indicates comprehensive agreement. We discuss MIPAS-STR in its current configuration, the spectral and radiometric calibration of the measurements and the retrieval of atmospheric parameters from the spectra. The MIPAS-STR measurements are significantly affected by continuum-like contributions, which are attributed to background aerosol and broad spectral signatures from interfering trace gases and are important for mid-infrared limb-sounding measurements in the Upper Troposphere/Lower Stratosphere (UTLS) region. Considering for continuum-like effects, we present a scheme suitable for accurate retrievals of temperature and an extended set of trace gases, including the correction of a systematic line-of-sight offset.

AMTD
4, 7035–7108, 2011

1 Introduction

Airborne and balloon-borne remote-sensing measurements are filling the gap between in-situ-measurements and satellite-borne remote sensing measurements in terms of spatial coverage and spatial resolution. While classical in-situ measurements from aircraft or balloon platforms allow for measurements with high absolute accuracy constrained to the flight track, satellite remote measurements allow for maximal vertical sampling range, global coverage and extended time series, but often with higher uncertainties. In contrast to comparable satellite techniques, remote-sensing measurements from aircraft and balloon platforms focus on limited atmospheric areas, but with a much higher sampling density. The proximity of the sampled air-masses results in lower uncertainties in the retrievals, since errors through pointing stability and precision, non-local thermodynamic equilibrium effects in the spectra and extended horizontal trace gas gradients are less severe. Further advantages of airborne high-altitude remote-sensing measurements are that flight scenarios can be adapted to scientific objectives individually and specific atmospheric structures can be targeted flexibly.

The cryogenic FTIR spectrometer MIPAS-STR (Piesch et al., 1996) onboard the high altitude aircraft M55 Geophysica is the airborne version of the series of MIPAS-instruments (Fischer and Oelhaf, 1996), including also ballon-borne (Friedl-Vallon et al., 2004) and satellite-borne techniques (Fischer et al., 2008). From the limb-emission measurements of MIPAS-STR, vertical profiles and two-dimensional cross-sections of atmospheric temperature and trace gases (HNO_3, O_3, CFCs, $ClONO_2$, H_2O and several other species) are derived, allowing for the reconstruction "snapshots" of the chemical and dynamical atmospheric situation along the flight-track.

MIPAS-STR was first deployed during the Antarctic campaign APE-GAIA in 1999 (Höpfner et al., 2000). In the following years, MIPAS-STR was operated in several other scientific campaigns and was applied for the validation of MIPAS-ENVISAT (Blom et al., 2004; Keim et al., 2004; Cortesi et al., 2007; Höpfner et al., 2007; Wang et al., 2007) and the microwave limb sounder MARSCHALS (Dinelli et al., 2009). The vertical

AMTD
4, 7035–7108, 2011

profile of peroxyacetyl nitrate (PAN) in the upper tropical troposphere was derived from measurements of MIPAS-STR (Keim et al., 2008). MIPAS-STR was recently operated during the RECONCILE campaign (Reconciliation of Essential Process Parameters for an Enhanced Predictability of Arctic Stratospheric Ozone Loss and its Climate Interactions, see https://www.fp7-reconcile.eu) in the Arctic Winter 2009/2010.

We describe the instrument in its current configuration and present results for RECONCILE flight 11 on 2 March 2010. An advanced retrieval approach is established, considering continuum-like effects, which significantly affect mid-infrared limb-emission spectra in the altitude-range sampled by MIPAS-STR. Retrieval results are shown for temperature and an extended set of trace gases. The results of MIPAS-STR are compared with results from in-situ-instruments and the mid-infrared limb-sounder CRISTA-NF, which were deployed onboard the Geophyisca simultaneously.

An overview of MIPAS-STR in its actual setup is given in Sect. 2. The spectral and radiometric calibration scheme is summarized in Sect. 3. The atmospheric situation and the applied sampling strategy during RECONCILE flight 11, as well as the cloud detection procedure from MIPAS-STR spectra are discussed in Sect. 4. Aspects of the retrieval are described in Sect. 5. The results and validation are discussed in Sect. 6 and conclusions are drawn in Sect. 7.

2 Instrument overview

MIPAS-STR is a cryogenic high-resolution FTIR-spectrometer, capable of the detection of the limb-emission spectra of atmospheric trace gases in the mid-infrared. The instrument is described in its previous configurations in Piesch et al. (1996), Kimmig (2001) and Keim (2002). Many aspects of the instrument are comparable to the ballon-borne instrument MIPAS-B2 (Friedl-Vallon et al., 2004) and in a certain extend also to satellite-borne instrument MIPAS-Envisat (Fischer et al., 2008). Since MIPAS-STR has been slightly modified and optimised compared to prior campaigns, an updated summary of the instrument characteristics is given together with a brief description

AMTD
4, 7035–7108, 2011

here.

The instrument is deployed onboard the high-altitude aircraft M55 Geophysica, allowing for flight altitudes of up to 20 km and operating ranges of around 3000 km. The typical airspeed of the Geophysica at stratospheric altitudes is about 700 to 750 km h^{-1}. MIPAS-STR is pointing towards the right hand side of the flight path (91° relative to nose of aircraft). Sampling is performed in limb-mode and upward-looking geometries, allowing for the subsequent reconstruction of vertical profiles and two-dimensional cross-sections of temperature and trace gases.

Basically, the instrument is set up by two main modules: the optics module includes the scan-mirror, the telescope, the interferometer and the detector unit. The electronics module consists of the data-processing and the instrument-control electronics. A schematic representation of the optics module is shown in Fig. 1 and the characteristics of the instrument in the actual setup are summarized in Table 1.

Infrared radiation from the probed airmass entering the instrument is directed via the scan-mirror into the telescope, the interferometer and the detector dewar subsequently. The main function of the 3-mirror telescope with an optical conversion ratio of 1.7 is the suppression of radiation from outside the field-of-view (FOV), which is scattered at surfaces inside the instrument or is diffracted at the edges of the front optics. The vertical FOV-extension is 0.44° (full cone). For the characterization of the instrumental line-shape (ILS), a theoretical model is applied instead of an experimental determination of the ILS. This approach has been found to be suitable for the ballon-borne instrument MIPAS-B2 (Lengel, 2004) and also shows reliable results for MIPAS-STR. Furthermore, Stiller et al. (2002) have shown for the case of MIPAS-Envisat that errors due to FOV- and ILS-effects are of minor importance in radiative modelling for this comparable instrument. However, the FOV shape of the instrument is characterized by calibration measurements on ground, and the resulting vertical FOV weighting function is considered in the retrievals to minimize possible uncertainties.

AMTD
4, 7035–7108, 2011

The effective optical path difference of the double pendulum interferometer (Fischer and Oelhaf, 1996) is ±13.9 cm. Two-sided interferograms are recorded, resulting in spectra with an unapodized spectral resolution of 0.036 cm^{-1}. After applying the Norton-Beer strong apodization (Norton and Beer, 1976), an effective spectral resolution of 0.058 cm^{-1} is obtained. The effects of vibrations, which are typical for an aircraft platform like the Geophyisca, on the interferometer of MIPAS-STR have been investigated by Kimmig (2001). A dedicated time-equidistant sampling method introduced by Brault (1996) was adapted for the recording of interferograms, such that perturbations in the spectra resulting from vibrations are minimized.

In order to minimize instrumental background radiation, the instrument is dry ice-cooled to about 210 K and the different reflective optics are coated with gold, protected gold or Silflex MK2^{TM}, respectively. The detector is cooled by liquid helium to about 4 K. Incoming infrared radiation is entering the detector dewar via an anti-reflectance coated ZnSe-window. Inside the detector dewar, the radiation is split up into four parts by dichroics and is directed via filters and blockers to the Si:As back-illuminated band-impurity detectors of the four channels. In this context, results from the spectral channel 1 (725 to 990 cm^{-1}) are discussed. For this channel, a typical plot of the apodized noise equivalent spectral radiance (NESR) under flight conditions is shown in Fig. 2. In the spectral range between 820 and 970 cm^{-1}, an optimal mean NESR of about 8×10^{-9} W/(cm^2 sr cm^{-1})) is obtained, and at lower and higher wave-numbers, the NESR is still mainly around 1 to 2×10^{-8} W/(cm^2 sr cm^{-1}).

The electronics module consists of a hierarchic system with intelligent and independent subsystems, realized by a transputer-network. The top system is a PC-based computer running a real-time operating system. Subsystems are the interferometer electronics, the line-of-sight (LOS) electronics and the housekeeping/auxiliary electronics. The system is designed for fully automatic operation during flight. On ground, the system can be accessed and commanded via Ethernet and during flight via an Iridium satellite link (see http://www.iridium.com/default.aspx).

AMTD
4, 7035–7108, 2011

Since the recording of a single interferogram takes about 9.5 s and the measurements are performed at fixed tangent altitudes, a reliable and accurate line-of-sight (LOS) stabilization is required for compensating roll-variations of the aircraft in order to minimize uncertainties in the trace gas retrievals. The development and verification of the LOS stabilization of MIPAS-STR is described by Keim (2002). The LOS elevation stabilization is realized by the scan-mirror control loop. The angle of the scan-mirror is measured by a 19-bit encoder and stabilized by a motor with reference to the attitude information provided by the Attitude and Heading Reference System (AHRS), which is part of the instrument. The AHRS is a Schuler-adapted, north-seeking strapdown inertial navigation system with embedded GPS and a 10 states Kalman-filter. The AHRS provides attitude angles at a data rate of 128 Hz and low data age, allowing for a near real-time LOS stabilization. After flight, the LOS data is refined by a dedicated post-processing procedure, compensating for drifts in the AHRS data.

Under flight conditions, a slight misalignment of the optical axis of the instrument with respect to the coordinate system of the AHRS can happen. The observed misalignment is mainly attributed to the exposure of the instruments housing to the large temperature difference between ground and stratosphere (in the order of 50 K). For the compensation of this effect, the offset of the LOS with reference to the AHRS coordinate system is quantified by LOS retrievals (see Sect. 5). The retrieved LOS offset is found to be approximately stable under the relatively constant flight-conditions in the stratosphere for individual flights. For each flight, one single LOS offset-parameter is determined and considered for the subsequent retrievals of temperature and trace gases. Including the uncertainties inherent to the AHRS, the accuracy of the scan-mirror adjustment and the uncertainties resulting from the LOS retrieval, a total pointing accuracy of 0.78 arcmin (1σ) is estimated. This value corresponds to about 3 % of the instrumental FOV or about 100 m at the lowest tangent altitude.

The sampling programme of MIPAS-STR includes atmospheric measurements and calibration measurements. The atmospheric measurements with negative elevation angles, which are characterized by their tangent altitude, allow for the retrieval of ver-

AMTD
4, 7035–7108, 2011

tically resolved profiles of atmospheric temperature and trace gases below flight altitude. Measurements with positive elevation angles allow for the retrieval of the column amounts of these parameters above the flight path and also contain limited information on the vertical distributions directly above flight altitude. In Fig. 3, the sampling scheme of the standard limb sequence is illustrated. The atmospheric measurements are enclosed by blackbody and deep space (zenith view) calibration measurements. Since the limb scans are aligned in a mirrored pattern, two full scans are shown. The standard sequence includes limb-viewing geometries with tangent altitudes between 5 km and the flight altitude (with a vertical spacing of 1 km above and 1.5 km below 8 km), an additional limb observation with an elevation angle of −0.3° in order to sample the area directly below the flight altitude, and comprehensive upward sampling. For a typical flight altitude of 18 km, one full limb scan of the standard limb sequence (including calibration measurements) takes about 3.8 min, corresponding to a flight path of approximately 45 km. The horizontal distances of the tangent points from the aircraft position increase from about 33 km for the highest geometry (tangent altitude 17.9 km, corresponding to an elevation angle of −0.30°) to about 400 km for the lowest geometry (tangent altitude 5 km, corresponding to an elevation angle of −3.54°). The vertical FOV diameter at the tangent point increases for the respective geometries from about 0.3 km to 3.0 km. Taking into account the vertical FOV angle of 0.44°, an oversampling with a factor of 2–3 is obtained for the limb-viewing geometries.

In the presence of opaque tropospheric clouds or in case of the requirement for an increased horizontal sampling density at higher altitudes, a modified measurement scenario is applied. Tangent altitudes below 9 km are omitted and upward-scanning is performed less frequently, resulting in a total time of about 2.4 min for one full limb scan, corresponding to a horizontal sampling of approximately 25 km.

AMTD
4, 7035–7108, 2011

3 Spectral and radiometric calibration

The spectral and radiometric calibration procedure is described in Höpfner et al. (2000) and Keim (2002) and is in many aspects similar to the procedure for the ballon-borne instrument MIPAS-B2 (Friedl-Vallon et al., 2004). In this context, a summary of the full calibration cycle specific to MIPAS-STR is given.

For the conversion of the atmospheric raw interferograms into radiometric calibrated spectra, basically four characteristic key-quantities have to be determined:

- The nonlinearity in the detector response
- The instrumental phase needed for the statistical phase correction within the Fast-Fourier-Transformation of the atmospheric interferograms into spectra
- The radiometric offset resulting from instrumental background radiation
- The gain-function for the radiometric calibration of the spectra

After the determination of these parameters, the atmospheric interferograms are transformed into spectra and are radiometrically calibrated according to the two-point calibration:

$$S(\nu) = \frac{A(\nu) - U(\nu)}{c(\nu)} \tag{1}$$

whereas ν stands for the spectral position, $A(\nu)$ for the atmospheric raw spectrum, $U(\nu)$ for the instrumental background spectrum, $c(\nu)$ for the radiometric gain function and $S(\nu)$ for the calibrated atmospheric spectrum. A schematic representation of the full calibration cycle is shown in Fig. 4 and the key-steps are described in the following sections in more detail.

For the correction of the detector nonlinearity, dedicated measurement phases are carried out during each flight, and the detector nonlinearity is considered to be approximately constant during an individual flight. After determination, the detector nonlin-

AMTD
4, 7035–7108, 2011

earity correction is applied to all interferograms of a flight prior to the other calibration steps.

For the subsequent steps phase correction, determination of instrumental offset, and radiometric calibration, an individual flight is separated into parts, where (i) the instrumental phase is sufficiently stable and (ii) the instrumental offset and (iii) the radiometric gain function show only approximately linear variations, since the instrumental phase is averaged and the latter two quantities are fitted linearly in time for the atmospheric measurements. Furthermore, the mentioned parameters are determined separately for each interferometer scan direction (forward/backward sweep are carried out alternatingly), and the atmospheric interferograms are calibrated separately for the different interferometer scan directions, since the data-acquisition is slightly different.

3.1 Detector nonlinearity correction

The Si:As back-illuminated band impurity detectors show a significantly nonlinear response at increasing photon fluxes, resulting in a distortion of the interferograms and artefacts in the associated spectra.

The quantification of the detector nonlinearity for the ballon-borne instrument MIPAS-B2 is described in Kleinert (2006) and is carried out analogously for MIPAS-STR. Accordingly, a measured nonlinear interferogram can be approximated by a polynomial function of linear interferograms. Hence, the corresponding uncorrected spectrum can be described as a convolution of the undisturbed spectrum with itself and shows higher order artefacts. The effects of nonlinearity can be deduced and corrected from the artefacts in blackbody spectra from interferograms without digital filtering data reduction as a function of the corresponding DC-level measured at the detector.

In the case of MIPAS-STR, during each flight at least one phase for the recording of interferograms without digital filtering data reduction is carried out. Depending on the availability of measurements of sufficient quality, between 15 and 30 interferograms are averaged typically for each interferometer scan direction and converted into spectra. The resulting two spectra are averaged again and from the final resulting spectrum,

AMTD
4, 7035–7108, 2011

the nonlinearity is quantified by the minimization of the corresponding artefacts according to Kleinert (2006). In the case of the channel 1 spectra of MIPAS-STR, the quadratic and cubic artefacts are clearly apparent and are minimized in the spectral interval from 30 to 280 cm^{-1} for the quadratic and in the interval from 2150 to 2900 cm^{-1} for the cubic artefacts. No signs of higher artefacts are found. Although the quadratic artefacts are outside channel 1 and a cubic artefact shows only weak influence in this spectral region, the difference in the detector responses between deep space spectra (low photon flux) and blackbody spectra (high photon flux) has to be considered to keep the two-point calibration valid. For RECONCILE flight 11 on 2 March 2010 discussed in this context, an 18 % lower response is found for a typical blackbody spectrum compared to a deep space spectrum.

3.2 Phase correction of the interferograms

Since different contributions of radiation arise from the atmosphere and the different optical components inside the instrument, complex spectra with a natural phase are resulting from the interferograms after the Fast-Fourier-Transformation (see Friedl-Vallon et al., 2004). Basically, atmospheric radiation and radiation resulting from the instruments optical components between the beamsplitter of the interferometer and the detector contribute to the real part of the spectrum, while the self-emission of the beamsplitter contributes mainly to the imaginary part. Due to the frequency-dependent signal propagation in time in the optical dispersive elements and the electronic components, as well as sampling shifts relative to the interferogram peak, phase errors are resulting. Since the beamsplitter emission gives rise to significant contributions in the atmospheric measurements, the standard method described by Forman et al. (1966) cannot be applied here. A dedicated approach suited for the phase correction for MIPAS instruments has been developed by Trieschmann et al. (1999). A characteristic instrumental phase is determined using blackbody calibration measurements and is then used as initial phase for a statistical phase correction of the atmospheric interferograms (see Fig. 4).

AMTD
4, 7035–7108, 2011

Following this approach, in the first step an initial mean instrumental phase is determined from the blackbody measurements of the corresponding flight part according to Forman et al. (1966). This step is applicable, since for the blackbody measurements the contribution of the beamsplitter emission is comparably weak. The resulting preliminary instrumental phase is then applied for the phase correction of the 5°/8°/10°-measurements (elevation angles depending on the sampling sequence), which show only weak atmospheric signatures and allow for the extraction of the beamsplitter emission in the imaginary part. The resulting imaginary spectra, which are characterized by the beamsplitter emission pattern, are then averaged and smoothed in order to reduce the noise level without affecting the broad signatures resulting from the beamsplitter emission. In the next step, the improved final instrumental mean phase is determined from the blackbody measurements according to Forman et al. (1966), taking into account the beamsplitter emission derived in the previous step. The resulting instrumental phase serves as starting point for the statistical phase correction of the deep-space and atmospheric interferograms. In the statistical phase correction (Trieschmann et al., 1999), (i) the correlations between the real and imaginary parts of the spectra are minimized, since these parts are theoretically absolute independent from each other and (ii) the variances in the imaginary parts are minimized, since no sharp line features are expected here.

After the phase correction, the real parts of the atmospheric spectra (negative and positive elevation angles), which are containing the atmospheric signatures of interest, and the deep space spectra, allowing for the extraction of the instrumental background radiation, are further processed in order to obtain finally calibrated atmospheric spectra.

3.3 Determination of instrumental offset and radiometric calibration

The instrumental offset in the real parts of the spectra is determined from the deep space spectra following the iterative scheme developed by Höpfner et al. (2000). Since the deep space spectra are obtained from zenith view observation geometries towards

AMTD
4, 7035–7108, 2011

cold space, only weak atmospheric rest-signatures are apparent, and further remaining contributions represent the instrumental background radiation. In order to reproduce the instrumental background with maximal accuracy, the remaining atmospheric rest-signatures are removed by a radiative transfer step with KOPRA/KOPRAFIT (see Sect. 5.1). For this step, calibrated deep space spectra are required and therefore, a preliminary calibration is applied. The atmospheric rest-signatures in the deep space spectra are removed by a line fitting step without radiative transfer, allowing for the determination of a preliminary instrumental offset. Using the preliminary instrumental offset, a preliminary radiometric gain function is determined from the blackbody measurements, allowing for the calibration of the deep space spectra. For the determination of the preliminary gain function, as well for the final gain function, the blackbody measurements are used at a reduced resolution of 0.5 cm^{-1}, in order to reduce the noise level without affecting the filter function.

In the radiative transfer step, the remaining weak signatures of CO_2, O_3, HNO_3 and H_2O are retrieved and then subtracted from the measured deep space spectra, resulting in the desired instrumental offset spectra.

With the knowledge of the instrumental offset, the final radiative gain function is determined from the blackbody measurements according to Eq. (2):

$$c(\nu) = \frac{BB(\nu) - U(\nu)}{B(\nu,T) \cdot e(\nu)} \tag{2}$$

whereas $c(\nu)$ represents the final radiative gain function, $BB(\nu)$ the blackbody spectrum, $U(\nu)$ the instrumental offset spectrum, $B(\nu,T)$ the Planck function of the temperature T and $e(\nu)$ the emissivity of the blackbody. With the knowledge of the precise instrumental offset and the radiative gain function, the atmospheric spectra are calibrated according to Eq. (1).

In Fig. 5, examples of calibrated atmospheric spectra are shown together with a calibrated deep space spectrum. The deep space spectrum and the spectra with high elevation angles indicate a flat baseline and show no signs of any significant radiometric

AMTD
4, 7035–7108, 2011

offset. For lower elevation angles, the spectral baseline is superimposed by overlapping signatures of trace gases and significant continuum-like contributions, which have to be considered in the retrievals.

4 Flight description

RECONCILE flight 11 was carried out on 2 March 2010, starting from Longyearbyen (Spitsbergen) at 09:35 UTC and landing in Kiruna (Sweden) at 13:35 UTC. The flight was designated as the second part of a double-flight from Kiruna to Longyearbyen and return, and was situated in the late phase of the polar vortex 2009/2010 after a vortex split in February. During the time of the flight, a compact vortex remnant was passing Spitsbergen coming from Canada, allowing for the sampling of aged vortex air and vortex filaments.

The vertical distribution of the tangent points of the MIPAS-STR observations along the flight track is shown in Fig. 6 (upward-viewing geometries not indicated) together with the cloud index. During the first part of the flight, the modified limb sequence omitting the tangent points below 9 km was carried out, in order to achieve a high horizontal sampling density in the vortex air. Beginning from 11:35 UTC, the standard sequence with tangent points down to 5 km was applied, in order to increase the vertical coverage.

According to Spang et al. (2004), the cloud index is derived from the spectra as the colour ratio between the microwindows 788.20 to 796.25 cm^{-1} and 832.30 to 834.40 cm^{-1} and is indicated colour-coded in Fig. 6. While spectra with cloud indices higher than 4 are assigned as cloud-free, cloud indices between 1 and 4 indicate partly cloud-affected spectra and values close to 1 indicate clearly cloud-affected spectra. Since the cloud index described in Spang et al. (2004) is derived for MIPAS and CRISTA (Cryogenic Infrared Spectrometers and Telescopes for the Atmosphere) spectra from satellite orbits and is defined for stratospheric altitudes, the threshold for cloud-affected spectra is likely to be slightly different for MIPAS-STR, especially at tro-

AMTD
4, 7035–7108, 2011

pospheric altitudes. In fact, further studies (not published) indicate, that MIPAS-STR spectra with cloud index 3 are still retrievable without constraints. However, in this context the conservative cloud index threshold of 4 is applied in order to avoid any significant cloud-effects in the retrievals. While in Fig. 6 clearly cloud-affected spectra (cloud-index close to 1) are only visible towards the very end of the flight at the lowest tangent points, spectra assigned as partially cloud affected (cloud indices between 1 and 4) are found for all geometries with tangent points below 8 km and the corresponding spectra are omitted in the retrievals.

In Fig. 7, the flight track is shown together with the distribution of the tangent points. Since MIPAS-STR is pointing to the right hand side of the Geophysica, during the first flight part before the turning point, the area in the south-east of the flight track was sampled. After the turn at approximately 82° N, the instrument was sampling the area west of the flight track. The altitude distribution of the tangent points reflects the fact, that lower tangent points are situated further away from the aircraft position.

In Fig. 8, the meteorological context during the discussed RECONCILE Flight 11 is shown. The potential vorticity map at 450 K (approximately coinciding with the flight altitude of the Geophysica between 10:00 and 12:00 UTC) shows the late vortex remnant coming from Canada, passing Spitsbergen with the lower edge from north-west. The map reflects the meteorological situation at 12:00 UTC, well coinciding with the time of the flight. As can be seen from Figs. 7 to 8, the Geophysica ascended from Longyearbyen at Spitsbergen into the Canadian vortex remnant. After the turn at approximately 10:30 towards the southward flight leg, different air-masses covering vortex air, vortex-edge air and extra-vortex air were passed subsequently. An extended vortex filament can be identified in Fig. 8 above the Atlantic western of Scandinavia, which is covered partially by the tangent points of MIPAS-STR during the southern flight part. It has to be noted that vortex air and extra-vortex air can contribute to individual spectra of MIPAS-STR at the same time as a consequence of the horizontal extended viewing geometries.

AMTD
4, 7035–7108, 2011

5 Retrieval

5.1 Retrieval method

The retrieval of the atmospheric parameters is carried out using the forward model Karlsruhe Optimized and Precise Radiative Transfer Algorithm (KOPRA) (Stiller et al., 2000) and the inversion module KOPRAFIT (Höpfner et al., 2001).

KOPRA is a dedicated fast line-by-line code for the modelling of spectra from high-resolution spectrometers. It allows for including both limb mode and upward scanning geometries together for the same retrieved profile. Simultaneously, the derivatives of the spectra with respect to atmospheric and instrumental parameters are calculated. Various atmospheric aspects of radiative transfer are supported, like non-spherical ray-tracing, refraction, aerosol-effects, line-mixing and non-local thermodynamic equilibrium. Instrumental aspects like finite FOV and ILS are also considered in forward modelling. The spectral lines of the target gases are modelled using the Voigt-Profile, and for species with unresolved spectral signatures, available cross-section data is applied.

Utilizing the analytical derivatives provided by KOPRA, the inversion algorithm KOPRAFIT allows for the fitting of the full set of observations of one scan in many microwindows simultaneously, resulting in the desired vertical profile or quantity of interest. For the inversion calculations in this context resulting in vertical profiles of atmospheric parameters, Gauss-Newton iteration subjected to Tikhonov-Phillips regularization (Tikhonov, 1963; Phillips, 2003) is applied:

$$\boldsymbol{x}_{i+1} = \boldsymbol{x}_i + \left(\mathbf{K}_i^T \mathbf{S}_y^{-1} \mathbf{K}_i + \gamma \mathbf{L}^T \mathbf{L}\right)^{-1} \left[\mathbf{K}_i^T \mathbf{S}_y^{-1} (\boldsymbol{y} - \boldsymbol{f}(\boldsymbol{x}_i)) + \gamma \mathbf{L}^T \mathbf{L} (\boldsymbol{x}_\mathrm{a} - \boldsymbol{x}_i)\right] \quad (3)$$

Here, i represents the iteration-index, $\boldsymbol{x}_i$ stands for the vector with the retrieval quantities, $\boldsymbol{x}_\mathrm{a}$ for the a priori-profile, $\boldsymbol{y}$ represents the vector with the measured radiances, $\mathbf{K}_i$ is the spectral derivatives matrix (Jacobian) with respect to the retrieved quantities, $\mathbf{S}_y$ the variance-covariance matrix of the measurements and $\boldsymbol{f}$ the forward-model. The Tikhonov-Phillips regularization is realized by the first-order regularization operator $\mathbf{L}$

AMTD
4, 7035–7108, 2011

(e.g. Steck, 2002) and the regularization strength is adjusted by the regularization parameter γ. An advantage of the applied Tikhonov-Phillips smoothing constraint is the fact, that systematic biases with respect to absolute values of the target parameters are avoided rather than using a climatological constraint. The resulting profiles are forced towards the shape of the a priori profile only (depending on the regularization strength) rather than to climatological absolute values (e.g. Steck, 2002). The regularization parameters for the target parameters temperature, trace gases and background-continuum are optimised individually, avoiding oscillations in the results and considering the differences between the measured and retrieved spectra.

5.2 Characteristics of continuum-affected spectra from the UTLS

The altitude range resolved by the measurements of MIPAS-STR is situated mainly in the UTLS region between 5 and 20 km. In this range, effects referred in this context as "continuum-like contributions" are important in the spectra and have to be taken into account in the retrievals. Typical greybody-like continua in the spectra are resulting from clouds, and significantly cloud-affected spectra are filtered according to the cloud index from Spang et al. (2004) described in Sect. 4. Possible reasons for further continuum-like effects (under nominal cloud-free conditions) in the spectra on the scale of retrieval microwindows are:

- Low concentrations of aerosol accumulated along the line of sight
- Broad spectral signatures of trace gases
- Spectral line-shape related effects

The first aspect includes effects from all types of aerosol. Ubiquitary stratospheric sulphur-containing aerosols are associated to the global Junge-Layer (Junge et al., 1961) and can result from volcanic eruptions (e.g. Arnold and Bührke, 1983), anthropogenic influences and biogeochemical sources (e.g. Hofmann, 1990; Andreae and

AMTD
4, 7035–7108, 2011

Crutzen, 1997). Different types of particles also can result from or nucleate on meteoritic material (e.g. Curtius et al., 2005). Polar Stratospheric Cloud (PSC) particles are formed during winter at high latitudes (e.g. Peter, 1997) and significantly affect mid-infrared limb-emission spectra. Typical spectral signatures of PSC constituents allow for the classification of PSC types (e.g. Höpfner et al., 2006). Also cirrus cloud particles affect mid-infrared limb-emission spectra (e.g. Spang et al., 2002) and the corresponding effects can be taken into account by dedicated radiative transfer models (Ewen et al., 2005). Further types of stratospheric aerosol-particles were measured by in-situ instruments, whereas the sources for some particle types remain unclear (e.g. Murphy et al., 1998). So in summary, there can be different aerosol-families present in the UTLS region under nominal cloud-free conditions, which are capable of affecting the MIPAS-STR observations.

Regarding the second point, continuum-like signatures on the scales of retrieval microwindows (typically several cm^{-1}) also result from large molecules with characteristic broad signatures in the spectra, which are not or inaccurately covered by radiative transfer modelling. Here, the availabilities of suitable climatological profiles, as well as accurate spectral line-data and cross-sections represent limiting factors. For example, the mixing ratios of the family of the halocarbons increase with decreasing altitude in the UTLS (e.g. Fabian and Borchers, 1981) and the comparably large molecules exhibit broad spectral signatures, whereas the variable vertical profiles and the available spectral data for radiative transfer modelling are uncertain in several cases. Further candidates with poorly known profiles are the broad family of aliphatic and aromatic hydrocarbons. Several species have already been identified by infrared remote-sensing instruments (e.g. Coheur et al., 2007; Razavi et al., 2011). For many further species there are also large uncertainties in the knowledge of the vertical profiles and the spectral line and cross-section data. Although many species alone give rise to only weak signatures below or close to the NESR of MIPAS-STR, the net-effect accumulated by many different species can significantly affect the observations. Therefore, continuum-like contributions have to be expected on scales of retrieval microwindows as a conse-

AMTD
4, 7035–7108, 2011

quence of incomplete radiative transfer modelling of broad trace gas signatures, especially towards lower observation geometries.

The third aspect results from the fact that in the considered altitude range in the UTLS significantly increasing pressure broadening of the spectral lines is observed with decreasing altitude. As a consequence of the increasing Lorentzian character of the spectral lines and the overall increase of many spectral signatures towards lower observation geometries, the overlap of adjacent spectral signatures increases. For the consideration of the effects of overlapping line wings, spectral signatures in an extended wavenumber-range of 25 cm^{-1} around the selected microwindows are taken into account in the retrievals discussed here. Influences of the extreme line-wings of very strong distant CO_2-lines and the non-Lorentzian behaviour of H_2O-lines are considered by dedicated continuum models included in KOPRA (Stiller et al., 2000). However, remaining broad continuum-like spectral signatures resulting from the incomplete modelling of overlapping spectral signatures cannot be ruled out. Virtually continuum-like contributions on the spectral baseline within a microwindow might also result from imperfect spectral modelling of adjacent spectral signatures using the Voigt model, since it does not always allow for a sufficient reconstruction of the observed spectral line shapes (e.g. Ciurylo, 1998; Boone et al., 2007; Schneider et al., 2011). However, we clarify that the retrieval of background-continuum does not correct imperfect spectral modelling of line shapes, but rather might partially compensate net-effects resulting from incorrectly modelled line-wings of adjacent spectral signatures.

Furthermore we mention, that also stray-light effects resulting from impurities on the instruments scanning mirror might result in spectral contributions possibly interpreted as continuum-like contributions. Although no explicit signs for significant stray-light contributions could be identified in the MIPAS-STR spectra discussed here, however, stray-light contributions cannot be excluded completely.

So in summary, different superimposed so-called continuum-like contributions play a role in UTLS mid-infrared limb-emission FTIR spectra, with increased importance towards lower altitudes. The sources for continuum-like effects are variable with altitude

AMTD
4, 7035–7108, 2011

and for different spectral regions, whereas a clear and quantitative separation is complicated. Therefore, the net-effect of continuum-like contributions in the measurements analysed here is quantified by the retrieval of a wave number-independent background continuum, allowing for a reliable reconstruction of the main target parameters. Of course it has to be considered, that the main retrieval target has to show a signature sufficiently differing from continuum-like behaviour in the spectral microwindow(s) chosen for the retrieval. Taking this into account, we show that the simultaneous reconstruction of wave number-independent background continuum is necessary in the discussed retrievals for achieving agreement between the measurements and the retrieved spectra, and that the retrieval results of the main targets are ascertained by in-situ measurements (Sect. 6).

In Fig. 9a, a measured spectrum with a tangent altitude of 12 km is shown, where significant continuum-like effects are apparent. Also shown are the corresponding retrieved spectra with and without continuum-retrieval. The retrieval without consideration of background continuum results in poor agreement between measurement and retrieval result, while the retrieved spectrum with simultaneous reconstruction of background continuum reproduces the measured spectrum well. Remaining differences in the residual exceeding the NESR-level are attributed to signatures of weakly interfering trace gases, which are not identified or incorrectly modelled using climatological profiles. Such effects of weakly interfering gases increase towards lower altitudes, but compared to the chosen signatures of the target gas, the resulting uncertainties are small and allow for a reliable reconstruction of the target profile, at least at stratospheric altitudes. In Fig. 9b, the retrieved continuum profile from the corresponding full limb scan is shown for this microwindow and retrieval.

5.3 Retrieval approach

The full retrieval chain applied for the subsequent reconstruction of the LOS offset, temperature profiles and trace gas profiles is summarized in Fig. 10. As pointed out in Sect. 2, for MIPAS-STR the relative pointing information is known with high precision

AMTD
4, 7035–7108, 2011

due to the high accuracy of the attitude angles provided by the AHRS. Only a small constant absolute offset between the reference system of the AHRS and the instruments LOS has to be quantified by retrievals. Therefore, the first step in the applied retrieval chain is the determination of the LOS offset using strong isolated CO_2-lines in the spectra. For each sequence of a flight, an individual LOS offset parameter is retrieved, and the average of all retrieved LOS offset parameters is used as LOS correction, resulting in one single parameter per flight. Thereby, the following assumptions are made: (i) the temperature and pressure profiles used for the LOS retrieval, which are interpolated from the ECMWF T106 grid-point analysis, are correct on average during a flight. (ii) The applied CO_2-profile and spectral line data for the modelling of the CO_2-lines are also sufficiently accurate. (iii) Further significant errors e.g. resulting from uncertainties in the relative LOS-information (due to the limited accuracy of the AHRS data) or radiometric calibration show no significant systematic behaviour during a flight. (iv) The LOS offset is approximately constant during a flight.

Since an extended set of typically 50 to 70 limb sequences is available for a single flight and different air-masses along hundreds of kilometres are sampled, the effects of the uncertainties of the temperature and pressure profiles interpolated from ECMWF and of the CO_2-profile are expected to compensate for the average LOS offset. The atmospheric profile of CO_2 is well known, and weak variations in the low percent range have only small impacts on the LOS retrieval. Further errors resulting from the limited accuracy of the spectral line data, the relative LOS knowledge and the radiometric calibration are also expected to compensate on the timescale of flight, whereas remaining systematic contributions cannot be ruled out fully. However, severe systematic errors propagated into the LOS offset correction are expected to result in significant systematic errors in the majority of the subsequent trace retrievals and would alter the agreement with in-situ measurements, which is not observed (see Sect. 6). An approximately constant behaviour of the LOS offset under flight conditions is plausible, since the instrument is exposed to relatively constant temperatures during flight in the stratosphere.

AMTD
4, 7035–7108, 2011

In the next step indicated in Fig. 10, temperature is retrieved for all limb sequences, using the same spectral signatures with strong isolated CO_2-lines as for the LOS retrieval. The lines fulfil the requirements/advantages for a temperature retrieval of (i) strong intensity, (ii) being clearly separable from other spectral signatures, (iii) different opacity and (iv) different temperature-dependence. It has to be noted, that the absolute situation (i.e. position in altitude) of the retrieved temperature profiles is clearly affected by the previously determined LOS correction relying on interpolated temperature profiles from ECMWF and making use of the same spectral signatures as the temperature retrieval. But on the other hand, only one single constant LOS correction is applied for all limb sequences of a flight, and no vertical information within the profile is retrieved from the CO_2-signatures in the determination of the LOS correction. In contrast, mainly the information on vertical variability of the profile is derived from the CO_2-signatures in the temperature retrieval. In Sect. 6 we show that the retrieved temperatures represent an improvement compared to the interpolated ECMWF temperatures.

According to Fig. 10, the different trace gases are retrieved subsequently in the following steps. First, target gases with dominant signatures and low spectral interference with other species are retrieved; then, with the optimised knowledge of the profiles of these gases, the corresponding spectral signatures are modelled for the retrieval of further trace gases with signatures influenced by the previously retrieved gases. Using previously fitted fixed profiles of significantly interfering species rather than climatological profiles allows for an improved modelling, since atmospheric variability is taken into account. This is especially important, when spectra of air-masses from different origin (e.g. vortex and extra-vortex air) within single limb scans are retrieved. If possible, the simultaneous reconstruction of interfering gases is avoided, since the total number of fit-parameters is increased and the simultaneous reconstructed parameters can potentially compensate each other to a certain extend (depending on the shapes of the individual signatures and the selected microwindows), especially in the context of the continuum-retrieval. Hence, the previous accurate retrieval of the interfering species

AMTD
4, 7035–7108, 2011

making use of strong separate signatures and keeping the corresponding profiles fixed in subsequent retrievals is preferred. For weakly interfering gases (with signatures close to the noise-level of the spectra), climatological profiles are applied for spectral modelling.

Following this approach (compare Fig. 10), first HNO_3 is retrieved, for which strong isolated signatures are available, characterised by only very weak known interference with other trace gases. Under consideration of the retrieved HNO_3-profiles, O_3 and CFC-12 are retrieved in the next stage. The retrieved HNO_3- and O_3-profiles are then considered for the retrievals of CFC-11 and $ClONO_2$. Finally, H_2O is retrieved under consideration of the retrieved HNO_3-, O_3- and $ClONO_2$-profiles. The vertical profile of H_2O shows a strong tropospheric gradient in contrast to the only weakly varying stratospheric mixing ratios. Therefore, logarithmic inversion is applied, resulting in more reasonable results in this particular case than the linear inversion applied for the other retrievals. It has to be mentioned, that for the other retrieval target parameters microwindows with no significant spectral interference with H_2O signatures are used, since several signatures of H_2O strongly increase towards tropospheric altitudes and complicate retrievals of other parameters.

5.4 Retrieval setup

For the retrievals, a grid between 0–100 km with a spacing of 0.5 km below 30 km and increasing spacing above is applied. Regularization is needed, since the applied retrieval grid in the vertical range of interest (spacing of 0.5 km) is finer than measurement grid (mainly spacing of 1 km) and the vertical FOV of the instrument. However, considering the complex combination of (i) the increase of the vertical FOV diameter with decreasing tangent altitude, (ii) oversampling, (iii) the non-strictly conducted 1 km-sampling grid in the specific limb programs, (iv) the corrected LOS variations quantified in the AHRS-post-processing altering the sampling grid, and (v) the effects of the inhomogeneous vertical FOV, the combination of a 0.5 km retrieval grid with an optimized regularization is found to allow for a comprehensive use of the vertical information in-

AMTD
4, 7035–7108, 2011

cluded in the spectra. The regularization strength is adjusted as small as possible to make maximal use of the information in the spectra and simultaneously avoiding oscillations in the retrieved vertical profiles.

The utilized spectral microwindows for the retrievals and the most prominent target signatures are summarized in Table 2. Spectral line parameters and cross-sections for the retrievals are taken from the MIPAS database (Flaud et al., 2002, 2006). Only for $ClONO_2$, cross-section data is taken from a study of Wagner and Birk (2003). Depending on the availability of suited microwindows with sufficiently strong target signatures and low spectral interference with other gases, each 1 or 2 microwindows are selected for the individual retrievals, allowing for manageable and efficient optimization of the regularization parameters and fast computation. Retrieval parameters are (i) the target quantity (LOS offset/temperature/trace gases), (ii) wave number independent background continuum for each microwindow and (iii) spectral shift of the microwindows. As mentioned before, the simultaneous reconstruction of further trace gases beside the target quantity is avoided, if possible. From the cases discussed here, only in the retrieval of the LOS correction and in the temperature retrieval O_3 is reconstructed as additional parameter. However, the corresponding signatures are clearly separable from the target-signatures of CO_2, allowing for a reliable reconstruction of the main target parameter (the results for O_3 with comparably low accuracy and vertical resolution are discarded subsequently). Regularization is applied to the retrieval parameters temperature, trace gases and background continuum.

In the individual retrievals, the first step is the optimization of the background continuum regularization strength for high vertical resolution, keeping the regularization of other retrieved quantities (trace gases/temperature) at a conservatively chosen fixed strength. In the next step, the optimized regularization strength for the background continuum is kept fixed and the regularization strength for the target quantity is optimized for high vertical resolution. Regularization parameters are optimized for a representative limb sequence and are subsequently kept constant for all limb sequences of a flight.

AMTD
4, 7035–7108, 2011

Pressure profiles for all retrievals are interpolated from the ECMWF analysis at T106 resolution. Since the retrieval of the LOS correction is carried out prior to the temperature retrieval, temperature profiles for the LOS retrieval are also interpolated from the ECMWF T106 analysis. For the subsequent trace gas retrievals, the retrieved temperature profiles are taken into account.

In all discussed retrievals, initial guess and a priori profiles are identical for an individual retrieval parameter. For the temperature retrievals, the interpolated profiles from ECMWF are used as initial guess/a priori profiles. For the trace gas retrievals, the initial guess/a priori profiles are taken from the Polar Winter Profiles for MIPAS V3.1 of Remedios et al. (2007), slightly modified for the conditions of the Polar Winter 2009/2010 (i.e. CO_2 mixing ratios updated). For the reconstruction of background continuum, the initial guess/a priori is set to zero, starting the retrieval with the assumption of no continuum. Signatures of weakly interfering trace gases which are not retrieved are considered by their climatological profiles from Remedios et al. (2007).

5.5 Retrieval result characterization

The retrieval results are characterized by the following quantifiers: (i) estimated error, (ii) vertical resolution and (iii) degrees of freedom. Different error-sources inherent to the measurement technique and the retrieval method are divided into two groups. The dominating errors, assigned as "primary errors", are resulting from:

- uncertainties in the spectroscopic line data
- uncertainties of the applied temperature profiles
- uncertainties of the LOS-information
- radiometric calibration errors
- spectral noise

Further errors sources referred as "secondary errors" are

AMTD
4, 7035–7108, 2011

- uncertainties in the applied pressure profiles
- uncertainties resulting from horizontal inhomogeneities in the atmosphere
- uncertainties in the retrieved/climatological trace gas profiles used for forward-modelling of interfering species
- uncertainties of trace gas profiles above the flight path
- errors due to non-local thermodynamic equilibrium at high altitudes
- line-mixing of spectral signatures
- errors in the characterization of the FOV
- deviations of the real ILS from the theoretical model
- errors resulting from the limited knowledge of the aircraft altitude (GPS)
- errors resulting from stray-light in the instrument
- further errors resulting from the electronic data acquisition chain

The primary errors are considered in the error estimation, while the secondary errors are expected to be of minor importance in most cases and are not included in the error-budget. Uncertainties of the interpolated pressure profiles are expected to have low impact as a consequence of the high quality of the ECMWF data. Errors due to the non-consideration of horizontal gradients of atmospheric parameters along the line-of-sight are expected to be less important compared to the ballon-borne and satellite-borne MIPAS instruments as a consequence of shorter light paths through the atmosphere. However, in the presence of strong horizontal gradients and contrasts of trace gas mixing ratios, significant uncertainties in the retrievals cannot be excluded, since in the retrieval constant atmospheric conditions are assumed for single limb scans. On the other side, to limited extent, the effects of horizontal gradients in the retrievals can

AMTD
4, 7035–7108, 2011

also be interpreted as a characteristic of the sampled air-mass as a whole rather than an error. Further uncertainties can arise from horizontal inhomogeneities along flight track, since spectral contributions from a certain altitude regime can change within the recording of a limb sequence, but significantly affect different measurement geometries of the same sequence.

Errors resulting from potentially inaccurate modelling of interfering signatures using retrieved and climatological profiles are expected to be of minor importance, since spectral microwindows with dominating signatures of the target gas and weak signatures from known interfering gases are utilized. Furthermore, errors in the modelling of broad and weakly structured interfering signatures are at least partially compensated by the retrieval of background-continuum.

The limited knowledge of the profiles of atmospheric constituents above the flight path represents a relevant error source in principle, especially in the case of trace gases where the maximum of the profile is located above the flight altitude. However, this uncertainty is reduced by considering the upward-viewing geometries included in the limb sequences, allowing for the reconstruction of column information above the flight path and to a limited extend also vertical information.

Errors resulting from non-local thermodynamic equilibrium are expected to be practically insignificant for the measurement geometries of MIPAS-STR, since these effects are mainly important high above the flight altitude (e.g. Manuilova et al., 1998; von Clarmann, 2003). Possible errors resulting from line-mixing (e.g. Funke et al., 1998) are minimized by choosing microwindows without significant Q-branches. The minor importance of FOV and ILS related uncertainties is discussed in Sect. 2.

It has to be noted, that the error resulting from the knowledge of the flight altitude can become important especially in ascent and descent phases, since the aircraft changes the flight altitude with several meters per second, and the GPS altitude information (which is also uncertain within several tens of meters) has to be interpolated to the mean time of an interferogram. Stray-light related errors were investigated by Keim (2002) for flights with strong particle contamination on the scan mirror of MIPAS-

AMTD
4, 7035–7108, 2011

STR. During the RECONCILE campaign, no strong particle contamination of the scan mirror was observed and stray-light related effects were not identified. However, weak stray light contributions cannot be fully excluded. Significant errors resulting from the electronic data acquisition chain are not identified.

As described in Rodgers (2000), another relevant error in principle is the smoothing error, indicating the uncertainties resulting from the limited vertical resolution of the retrieval result. In case of Tikhonov-Philipps regularization, the smoothing error expresses the retrieval error due to smoothing as a consequence of regularization (e.g. von Clarmann, 2003). Following Rodgers (2000), no smoothing error is estimated for the shown MIPAS-STR results, since in most cases no estimate of the true ensemble covariance of suited accuracy (i.e. a climatological covariance matrix) needed for the calculation is available. Especially in the discussed flight, structured and overlapping air-masses from different origin are covered by the measurements of MIPAS-STR, and the estimation of a representative climatological covariance matrix is practically not possible. Following Rodgers (2000), the retrieval result is considered as an estimate of the smoothed version of the state rather than an estimate of the complete state, which has to be kept in mind when interpreting the retrieval results.

For the retrieval of the LOS correction, in principle all errors listed above under "primary errors" are relevant for the determination of the individual LOS offsets. But since the LOS offset is estimated as the average of a large number of limb sequences (61 for RECONCILE flight 11), the different errors are expected to compensate each other. In Fig. 11, the retrieval results for the individual LOS offsets are shown for the whole flight. The values are scattering well around a mean LOS offset of 5.45 arcmin with a 1σ-uncertainty of 0.19 arcmin. Outliers can be caused by the availability of low numbers of quality-filtered observation geometries, and/or different combinations of the individual error sources listed above. The outliers associated to the first sequence and the last sequences belong to ascent and descent phases, where the flight altitude is changing fast, resulting in additional uncertainties of the sampling geometries. As can be seen in Fig. 11, the found LOS offset is approximately constant during the flight,

AMTD
4, 7035–7108, 2011

and using the average LOS offset as correction for all limb sequences seems to be appropriate. The uncertainty of the corrected LOS is calculated taking into account the 1σ-uncertainties resulting from (i) the attitude information from the AHRS after postprocessing of 0.75 arcmin, (ii) errors resulting from the scan-mirror control of 0.09 arcmin and (iii) the 1σ-uncertainty of the derived mean LOS correction of 0.19 arcmin. The uncertainties are combined by the root of the square sum, resulting in an estimated LOS-uncertainty of 0.78 arcmin. Hence, the LOS-uncertainty, which is used for the estimation of the LOS-associated uncertainties in the following retrievals, is dominated by the accuracy of the post-processed attitude information provided by the AHRS.

The error of to the temperature retrieval is estimated according to Wetzel et al. (2002) for the balloon-borne MIPAS instrument. The effects of spectroscopic line data errors and uncertainties of the applied CO_2-profile are estimated by retrievals with a shifted CO_2-profile (5 %). LOS-related errors are estimated by retrievals taking into account of the LOS-uncertainty (0.78 arcmin), and radiometric calibration errors are considered by retrievals with modified gain (2 %). The corresponding errors for retrieved temperature profiles are calculated as the differences between the retrieval results with the modified quantity and the initial retrieval results according to

$$\Delta \boldsymbol{x}_j = \begin{pmatrix} \Delta x_{1,j} \\ \Delta x_{2,j} \\ \vdots \\ \Delta x_{n_{\max},j} \end{pmatrix} = (\mathbf{K}^T \mathbf{S}_y^{-1} \mathbf{K} + \gamma \mathbf{L}^T \mathbf{L})^{-1} \mathbf{K}^T \mathbf{S}_y^{-1} (\boldsymbol{y}_{\text{error},j} - \boldsymbol{y}_{\text{result}}), \quad (4)$$

whereas $\Delta \boldsymbol{x}_j$ represents the vertical error profile resulting from the modified quantity j, $\Delta x_{n,j}$ the errors at the altitude levels n, $\boldsymbol{y}_{\text{error},j}$ the calculated spectrum with the modified quantity and $\boldsymbol{y}_{\text{result}}$ the calculated spectrum of the initial retrieval result (von Clarmann, 2003). Together with the spectral noise error, the resulting error vectors are combined to the estimated 1σ-uncertainty for temperature by the root of the square-sum according to:

$$\Delta \boldsymbol{x}_T = \sqrt{\Delta \boldsymbol{x}^2_{\text{prof,spec}} + \Delta \boldsymbol{x}^2_{\text{los}} + \Delta \boldsymbol{x}^2_{\text{cal}} + \Delta \boldsymbol{x}^2_{\text{noise}}}, \quad (5)$$

AMTD
4, 7035–7108, 2011

whereas $\Delta \boldsymbol{x}_T$ represents the estimated error vector of the retrieval result. The individual error contributions $\Delta \boldsymbol{x}_{\text{prof,spec}}$, $\Delta \boldsymbol{x}_{\text{los}}$ and $\Delta \boldsymbol{x}_{\text{cal}}$ are resulting from the retrievals with the modified CO_2-profile, LOS and gain, and $\Delta \boldsymbol{x}_{\text{noise}}$ represents the spectral noise error. The estimated error of the retrieved temperature is used in the following retrievals for the determination of the corresponding temperature-related errors.

Following Wetzel et al. (2002), for the trace gas retrievals the spectroscopic errors (line data and cross-sections) are estimated to conservative constant percentages of the absolute profile values. The spectroscopic error of 8 % for HNO_3 is taken from Wetzel et al. (2002). Considering the results of Moore et al. (2006), for CFC-11 and CFC-12 spectroscopic errors of 10 % are taken into account. For ozone, a spectroscopic error of 7 %, and for H_2O, a spectroscopic error of 10 % is adopted, considering the uncertainties for the line intensities of the target signatures (Flaud et al., 2002, 2006 and references therein). For the $ClONO_2$ cross-section, the worst case error of 5.5 % reported by Wagner and Birk (2003) is considered. The errors for the trace gas retrievals due to the uncertainties of temperature, LOS and radiometric gain are also estimated according to Eq. (4) by retrievals with the corresponding modified quantities. The estimated 1σ-errors for the trace gas profiles are calculated according to

$$\Delta \boldsymbol{x}_{\text{vmr}} = \sqrt{\Delta \boldsymbol{x}_{\text{spec}}^2 + \Delta \boldsymbol{x}_T^2 + \Delta \boldsymbol{x}_{\text{los}}^2 + \Delta \boldsymbol{x}_{\text{cal}}^2 + \Delta \boldsymbol{x}_{\text{noise}}^2} \tag{6}$$

with $\Delta \boldsymbol{x}_{\text{vmr}}$ the estimated error vector of the retrieval result, $\Delta \boldsymbol{x}_{\text{spec}}$ the spectroscopic error and the other contributions as in the case of the temperature error.

It has to be considered, that the different error sources can show variations on different timescales. While e.g. the noise error is characteristic for single spectra (recording of one interferogram takes approximately 9.5 s), temperature-related errors can be relevant for full limb scans (a few minutes) and spectroscopic errors might affect entire flight sections. As a consequence, the combined error might show a more systematic behaviour in particular flight parts and the statistical combination of the errors has to be seen with suspicion. The discussed error-budget reflects the attempt to give one single

AMTD
4, 7035–7108, 2011

error quantity summarizing all of the discussed effects. However, the applied strategy results in reasonable errors, as indicated by the in-situ comparisons in Sect. 6.

The vertical resolution of the retrieval results is derived from the averaging kernel matrix **A** (Rodgers, 2000):

$$\mathbf{A} = (\mathbf{K}^T\mathbf{S}_y^{-1}\mathbf{K} + \gamma\mathbf{L}^T\mathbf{L})^{-1}\mathbf{K}^T\mathbf{S}_y^{-1}\mathbf{K} \quad (7)$$

According to Purser and Huang (1993), the reciprocal of the peak of **A** can be taken as a measure of its width, which is often used as a measure of the vertical resolution of a retrieval result. We calculate the vertical resolution Δa_n at the altitude n as the absolute value of the quotient of the local vertical grid spacing Δh_n divided by the trace element $\mathbf{A}_{n,n}$:

$$\Delta a_n = \left| \Delta h_n / \mathbf{A}_{n,n} \right| \quad (8)$$

The degrees of freedom (DOF) of the retrieval result are the sum of the trace elements of **A** and indicate how many independent pieces of information are derived from the measurements allowed by the regularization (e.g. Steck, 2002). In the case of MIPAS-STR, weak regularization results in DOF close to the number of observation geometries with tangent altitudes (containing the majority of vertical information). With regard to the DOF, the upward scanning geometries can be considered in a simplified way like a single additional geometry with the characteristics a nominal geometry with tangent altitude. Strongest regularization of first order would result in DOF close to 1.

In the left panel of Fig. 12, the retrieval result for a single HNO_3 profile is shown together with the estimated 1σ-error. The initial guess/a priori profile used for the retrieval is also shown. The retrieval result is very distinct from the initial guess/a priori profile and reflects the weak regularization strength. In the retrieved profile, a HNO_3-maximum at about 15 km with decreasing HNO_3-mixing ratios above is identified, which can be assigned to re- and de-nitrification layers at the edge of the polar-vortex (see Sect. 6.3).

The contributions of the different error sources are shown in the panel in the middle. Between flight altitude and the lowest tangent point, the dominating error source is

AMTD
4, 7035–7108, 2011

the uncertainty of the spectroscopic data, followed by the errors resulting from the radiometric calibration and the uncertainties of the retrieved temperature profiles. The LOS error is variable with altitude, and is together with the spectral noise error of minor importance. For sequences with more extended vertical coverage, all estimated errors except of the assumed spectroscopic line data error significantly increase towards the lower observation geometries, and the LOS error and the spectral noise error can become the dominating errors.

For the shown result, the estimated error is between 9 to 12 % in the altitude range between flight altitude and the lowest tangent point. Above flight altitude, the absolute numbers of all errors except of the spectroscopic error still decrease virtually, but this has to be interpreted in context of the vertical resolution indicated in the right panel. For the measurement geometries between flight altitude and the lowest tangent point, a high vertical resolution of mainly between 1 and 1.5 km is achieved due to the availability of comprehensive vertical information included in the spectra with negative elevation angles. Therefore, the estimated error is representative in this altitude range in the context of the vertical resolution. From the geometries with positive elevation angles, mainly column information is obtained for the atmosphere above the aircraft, and the vertical resolution rapidly decreases. Hence, for the parts of the retrieved profiles above the aircraft, the absolute numbers of the errors still decrease, but the vertical information is "smeared" over a broader vertical range. Practically only column information is obtained above 17.5 km and the errors become physically meaningless. At altitudes below approximately 8.5 km, which are not covered by the measurements, no vertical information is obtained, as indicated by the vertical resolution tending to infinity.

For the HNO_3-profile shown in Fig. 12, 8.7 DOF are obtained, which have to be interpreted in the context of the 9 tangent altitudes in the vertical range between 8.9 and 16.7 km plus two upward scanning geometries carried out in the modified limb sequence, indicating weak influence of the regularization. For higher flight altitudes, resulting in scans with more tangent altitudes, and scans with increased vertical coverage (as in the standard sequence), the numbers of DOF increase. The shown profile

AMTD
4, 7035–7108, 2011

represents the result for HNO_3 for an individual limb scan, and the corresponding errors are varying from scan to scan, depending on the atmospheric situation, the vertical distribution of the target species, and the sampling geometries. Whereas in most cases, the spectroscopic error represents the dominating error, the relative importance of the different error contributions can vary depending on the retrieval target.

6 Results

6.1 Approach for comparison of MIPAS-STR results and in situ measurements

Several in-situ instruments were deployed onboard the Geophysica during the RECONCILE campaign, allowing for comparisons with the MIPAS-STR results (Table 3). High precision ambient temperature measurements were obtained from the Thermodynamic Complex (TDC). Ozone measurements were taken by the Fast-Response Chemiluminescent Airborne Ozone Analyzer (FOZAN). CFC-11 and CFC-12 measurements were provided by the High Altitude Gas AnalyzeR (HAGAR). Gas-phase water vapour measurements were obtained by the Fluorescent Lyman-alpha Stratospheric Hygrometer for Aircraft (FLASH-A), which is a recent modification of the previously utilized FLASH instrument on board of the Geophysica aircraft (Sitnikov et al., 2007).

For the discussed flight, MIPAS-STR measurements of high spatial coincidence with the in-situ measurements related to the ascent phase of the Geophyisca are available (Fig. 13). The lowest tangent point of the selected scan 02_01788 is located at an altitude 8.9 km and the flight altitude is 16.7 km, whereas 9 limb-viewing and 2 upward-viewing geometries were carried out. The two tangent points located spatially closest to the flight path during ascent correspond to tangent altitudes of 14.0 and 15.1 km. For comparisons, it has to be considered that the airvolume sampled by MIPAS-STR during one limb sequence (duration typically a few minutes) covers horizontally several tens of kilometres along flight track and several hundreds of kilometres along the viewing direction (see Sect. 2) and the vertical resolution is limited compared to in-situ

AMTD
4, 7035–7108, 2011

measurements. In contrast, the in-situ measurements giving rise to the ascent profile are carried out in a more extended time interval (about half an hour) and provide precise measurements at certain altitudes and positions. The limited temporal coincidence (time mismatch ca. 1 h) between the MIPAS-STR measurements and the in-situ measurements has also to be reminded, since chemical and dynamical atmospheric structures can move or change in the time between the measurements.

The retrieval results at flight altitude are compared to the in-situ measurements along flight track for flight sections with approximately constant flight altitude. Three different flight sections with approximately constant flight altitude are situated between 10:05–11:25 (I), 11:25–12:05 (II) and 12:05–12:45 (III) UTC (Fig. 6). The in-situ measurements are compared to the retrieval results at the grid-altitudes 17.0, 17.5 and 19 km, respectively.

As discussed in Sect. 4, the edge of the late Canadian polar vortex remnant was located above Spitsbergen at the date of RECONCILE flight 11. During the ascent phase, the in-situ instruments sampled subsequently air below and inside the vortex. During the recording of scan 02_01788, MIPAS-STR was pointing into a region at the vortex edge, partially overlapping with the in-situ ascent profile (compare Figs. 8 and 13). At higher profile altitudes the in-situ measurements are located closer to the core region of the vortex remnant compared to the MIPAS-STR tangent points.

6.2 Retrieval results and in-situ comparison

The retrieval results for scan 02_01788 of MIPAS-STR are shown together with the corresponding in-situ measurements in Fig. 14a–f). In the case of $ClONO_2$, no suited in-situ measurements are available for comparisons, but the retrieval result is also discussed for completeness. For the retrieved profiles, the estimated 1σ-error, vertical resolution and DOF are indicated. Retrieved profiles and in-situ results are shown with reference to geometric (GPS-) altitude. Adapted ECMWF-data (temperature and pressure) refer to geopotential height, with is comparable to geometric altitude in the

AMTD
4, 7035–7108, 2011

considered vertical range to a good approximation.

For the in-situ measurements, also profiles smoothed with the corresponding averaging kernels of MIPAS-STR are shown (Rodgers, 2000). This approach allows for the comparison of the results of MIPAS-STR with the in-situ measurements at the common vertical resolution of MIPAS-STR. The in-situ result is transferred into an equivalent of the estimate of a smoothed state of the atmosphere as performed in the MIPAS-STR retrieval. In the case of temperature, also the interpolated profile from ECMWF is shown, which serves as initial guess/a priori profile for the retrieval. For the trace gases, the corresponding climatological profiles serving as initial-guess/a priori profiles are also shown. For all profiles of MIPAS-STR shown in Fig. 14a–f, only profile points with a vertical resolution of better than 5 km are plotted.

As can be seen in Fig. 14a, for temperature the agreement of MIPAS-STR and TDC is mostly better than 1 K and the agreement is improved compared to the interpolated ECMWF-profile. In the upper part of the profile, the agreement between MIPAS-STR and TDC slightly decreases, which is attributed to the decreasing spatial overlap of the measurements. For O_3, also reasonable agreement is found between MIPAS-STR and FOZAN, as can be seen in Fig. 14b. The unsmoothed profile from FOZAN shows variable mixing ratios indicating horizontal structures in the O_3 distribution, especially between 12 and 14 km. In this altitude range, the retrieved profile from MIPAS-STR follows the upper part of the in-situ profile, while this structure is not apparent in the smoothed in-situ profile.

As can be seen in Fig. 14c and d, for CFC-11 and CFC-12 the results from MIPAS-STR and HAGAR are also mostly in agreement within 1 sigma of the estimated error below 15 km and 16 km, respectively. At higher altitudes, which are characterized by very low mixing ratios of the CFCs, the results start to diverge. This finding is attributed to the fact that the horizontally extended MIPAS-STR measurements here are significantly affected by spectral contributions from extra-vortex air with much higher mixing ratios of the CFCs. As will be shown below, the CFCs show by the far the strongest contrasts between vortex and extra-vortex air from the trace gases considered for in-

AMTD
4, 7035–7108, 2011

situ comparisons here.

In Fig. 14e, the results for H_2O from MIPAS-STR and FLASH-A are shown, and the instruments agree within the uncertainties. Slightly increasing differences below 10 km are attributed to the decreasing spatial overlap of the measurements and the tropospheric variability of H_2O. The retrieved profile of $ClONO_2$ is shown in Fig. 14f, where no in-situ measurements suited for comparisons are available. The retrieved profile indicates high $ClONO_2$-mixing ratios in the upper part of the profile, characteristic for the chlorine-deactivated air in the late vortex. Virtually negative mixing ratios below 10 km are a consequence of lowest mixing ratios of $ClONO_2$ in the troposphere and can result from predominantly additive combination of the discussed error sources. For gases with such weak signatures compared to the overall spectral background at tropospheric observation geometries, especially spectral interference with other trace gases not or incorrectly considered by climatological profiles can become important. However, we mention that the applied retrieval method does not constrain the result to positive values in order to avoid biases in statistics (von Clarmann, 2003). The corresponding retrieved profile for HNO_3 (for which also no in-situ comparison is performed) is discussed in Sect. 5.4 (Fig. 12).

For the shown retrieved profiles of the discussed scan, the estimated 1σ-errors are typically about 10–15 %. Typical vertical resolutions of 1 to 2 km are achieved in the altitude range of the tangent points. Between 6.4 and 8.7 DOF are obtained from the 9 limb-viewing and 2 upward-viewing geometries, indicating comprehensive vertical information in the measurements. For the continuum retrievals (not shown here) carried out for each microwindow simultaneously together with the target parameters, typically about 7 DOF are obtained for this scan. The shown retrieval results are nearly insensitive on the initial guess/a priori information as a consequence of the high signal-to-noise ratios of the measurements and the applied weak regularization.

The comparison of the retrieval results and the in-situ measurements along the flight track is shown in Fig. 15a–e. The retrieval results of MIPAS-STR for temperature are in very good agreement with the results of TDC (Fig. 15a) and the agreement is improved

AMTD
4, 7035–7108, 2011

compared to the interpolated ECMWF temperatures. As can be seen in Fig. 15b, for O_3 also reasonable agreement is found between MIPAS-STR and FOZAN.

The results of MIPAS-STR for CFC-11 and CFC-12 along the flight track are also in principle in agreement with the measurements of HAGAR (Fig. 15c and d), often already within one sigma of the errors. As in the case of the profile comparisons, higher mixing ratios of the CFCs are found in the first flight part for the MIPAS-STR results at flight altitude and are attributed to spectral contributions from outside of the polar vortex. The strong contrasts of the mixing ratios of the CFCs at the vortex edge can be seen consistently in the MIPAS-STR and HAGAR results in Fig. 15c and d. The vortex edge shows up in the HAGAR measurements sharply between 11:14 and 11:21 UTC by strong increases of the mixing ratios of CFC-11 and CFC-12 of 80 pptv and 180 pptv, respectively. In the case of MIPAS-STR, the corresponding structures appear more smoothly between 11:00 and 11:25 as a consequence of the different sampling characteristics. For comparison, the differences between vortex and extra-vortex air are less pronounced in the case of O_3 along the flight track, as consistently indicated by the results of MIPAS-STR and FOZAN (Fig. 15b). For CFC-11 and CFC-12, noticeable differences between the results of MIPAS-STR and HAGAR are found also especially in the last flight part (12:15–12:45) (Fig. 15c and d). The lower mixing ratios in the results of MIPAS-STR are explained by the fact that filaments of vortex air with lower mixing ratios of the CFCs were located along the instruments viewing direction in this particular flight part (compare Sect. 6.3), contributing to the spectra of MIPAS-STR. As can be seen in Fig. 15e, for H_2O reasonable agreement is found between the results of MIPAS-STR and FLASH-A.

The mean differences and the sample standard deviations of the mean differences between the results of MIPAS-STR and the in-situ measurements for the shown profile comparisons and comparisons along the flight track are summarized in Table 4. While the mean differences indicate systematic differences between the MIPAS-STR and the in-situ results, the sample standard deviations of the mean differences indicate the qualitative agreement for single retrieval-grid points. Both quantities together indicate

AMTD
4, 7035–7108, 2011

the quantitative agreement. In the case of the profile comparisons, these quantities are calculated taking into account the smoothed in-situ results at the retrieval-grid altitudes. For the comparisons along flight track, the unsmoothed in-situ results are interpolated in time for the MIPAS-STR retrieval results.

With mean differences of +0.2/−0.2 K for the profile and along-flight-track comparison, and respective sample standard deviations of about 0.7/0.6 K, the retrieved temperatures of MIPAS-STR agree very well with the TDC measurements within the uncertainties of the involved instruments. Also for O_3 excellent agreement is found between MIPAS-STR and FOZAN. The absolute mean differences between MIPAS-STR and HAGAR for CFC-11 and CFC-12 in the range of 8–21 pptv are also small. However, all mean differences calculated for the CFCs are positive, which is attributed to the extended first flight part with the MIPAS-STR measurements significantly biased by extra-vortex air. The corresponding percentages of the sample standard deviations of the mean differences (see Table 4) reflect the fact that the strong horizontal contrasts in the mixing ratios of the CFCs alter the comparability of the MIPAS-STR and HAGAR measurements. These comparably high values are mainly driven by the differences at high profile altitudes with very low absolute mixing ratios of the CFCs. However, this is masking the fact that the absolute mean differences and sample standard deviations for the CFCs are in the low ppt-range, indicating considerable agreement at higher mixing ratios of the CFCs (i.e. at lower profile altitudes). For the profile/along-flight-track comparisons for H_2O, the mean differences and corresponding sample standard deviations indicate agreement between the involved instruments.

To overcome the complications of the limited spatial overlap of the MIPAS-STR and HAGAR results in the context of the strong horizontal contrasts of the mixing ratios of the CFCs, in Fig. 16 the correlations of CFC-11 and CFC-12 derived from MIPAS-STR and HAGAR are shown. Collocated pairs of CFC-11 and CFC-12 measurements of the individual instruments are considered, whereas no spatial coincidence between the measurements of the two instruments is necessary. The resulting correlations show comprehensive agreement within the variability of the results of MIPAS-STR and the

AMTD
4, 7035–7108, 2011

associated uncertainties. Only for mixing ratios of CFC-11 between 30 and 150 pptv, slightly higher mixing ratios of CFC-12 are found for HAGAR, but the corresponding results are still within the variability of the MIPAS-STR results.

6.3 Two dimensional trace gas distributions

The retrieved vertical trace gas profiles obtained from the MIPAS-STR measurements are combined to 2-dimensional vertical cross-sections of the corresponding species along the flight track. In the upper panel of Fig. 17, the resulting vertical cross-section for HNO_3 is shown. In the first flight part between 10:00 and 11:15, at altitudes above 14.5 km, air of the late vortex edge can be clearly identified. A weak renitrification remnant is found with a HNO_3-maximum at 15.5 km and mixing ratios of about 8 ppbv, indicating between 2 to 3 ppbv higher mixing ratios compared to the layers above and below. The resolved vertical thickness of the layer is about 1 km, which is close to the vertical resolution limit of MIPAS-STR. Above, denitrified air characterised by low HNO_3-mixing ratios is found.

Between 11:35 and 12:00, a structure of extra vortex air can be identified, which is characterized by low HNO_3-mixing ratios below 16 km and shows no de-/renitrification-structure. The structure is diagonally linked to further structures of extra-vortex air in the last flight section with low HNO_3-mixing ratios, characteristic for extra-vortex air. In the last flight part, between 12:05 and 12:45, two prominent structures with strongly enhanced HNO_3-mixing ratios are apparent, which can be assigned to filaments of the polar vortex with renitrified air. HNO_3 mixing ratios of up to 10 ppbv are found for the lower structure centred at 14.5 km with a vertical extension of about 3 km, whereas the mixing ratio is about 5 ppbv increased compared to the surrounding air. The tiny upper structure located around 17.5 km with a vertical extension of about 1.5 km also shows significantly enhanced HNO_3 mixing ratios of up to 9 ppbv.

In Fig. 18, the corresponding vertical cross-section of HNO_3 derived from CRISTA-NF measurements is shown. CRISTA-NF is capable of the measurement of limb-emission spectra in a comparable spectral region like MIPAS-STR and is pointing

AMTD
4, 7035–7108, 2011

approximately into the same direction. The characteristics of CRISTA-NF are briefly summarized in Table 5 (e.g. Spang et al., 2008; Ungermann et al., 2011). While MIPAS-STR with its comparable high spectral resolution is able to separate weak trace gas signatures not resolved by CRISTA-NF, the advantage of CRISTA-NF is the higher vertical and horizontal sampling density allowing for the identification of atmospheric fine-structures not resolved by MIPAS-STR.

HNO_3 is retrieved from the CRISTA-NF measurements in the same spectral region as for MIPAS-STR and a typical vertical resolution of 0.5 km is obtained. For details concerning the CRISTA-NF retrieval, see Ungermann et al. (2011). As can be seen in Figs. 17 and 18, the retrieved vertical cross-sections of HNO_3 from the two instruments agree very well. All major structures observed in the MIPAS-STR result are also identified for CRISTA-NF: the de- and renitrification layers in the first part of the flight, the structure with extra-vortex air in the middle of the flight, and the vortex filaments in the last part of the flight. Several smaller substructures can also be identified in both results. It has to be noted, that the range of the colour-coding for CRISTA-NF in Fig. 18 is slightly higher than for MIPAS-STR in Fig. 17. Higher peak values observed in the CRISTA-NF result are consistent with atmospheric fine-structures with enhanced HNO_3-mixing ratios spatially higher resolved by CRISTA-NF. However, we emphasize that the measurements of the two limb-sounding instruments using different techniques and processed with different forward and inversion models are resulting in cross-sections with considerable agreement.

The vertical cross-section of CFC-11 from MIPAS-STR in Fig. 19 shows a complementary picture to the HNO_3 cross-sections: vortex air in the first flight part and vortex filaments at the end of the flight are characterised by low mixing ratios of CFC-11, while extra vortex air is indicated by increased mixing ratios of CFC-11 at stratospheric altitudes.

Some of the structures visible in the cross-sections of HNO_3 and CFC-11 are horizontally largely extended (like the renitrification remnant in the beginning, with an extension along flight track of about 500 km between the turning point and the vortex

AMTD
4, 7035–7108, 2011

edge) or show diagonally linked patters and further fine-structures.

7 Conclusions

In the work in hand, we present the FTIR limb-sounder MIPAS-STR deployed on the high altitude aircraft M55 Geophysica in its current performance. The applied calibration scheme from the measured data towards radiometrically calibrated spectra is discussed. A comprehensive bottom-up retrieval scheme for the reconstruction of temperature, HNO_3, O_3, CFC-11, CFC-12, $ClONO_2$ and H_2O is introduced, including the correction of a systematic line-of-sight offset. The significant influences of continuum-like effects on limb-emission mid-infrared spectra in the UTLS region and their treatment by the retrieval of wavenumber-independent background continuum on the scale of retrieval microwindows are discussed. Retrieval results are shown exemplary for RECONCILE flight 11 on 2 March 2010.

The estimated overall 1σ-errors of the retrieval results are below 1 K for temperature and typically between 10 and 15 % for the trace gases in the vertical range spanned by the tangent points. The vertical resolutions for the different target parameters are typically between 1 to 2 km in the vertical range of the tangent points and slightly above the flight path, allowing for the identification of narrow vertical structures. Depending on the sampling programme, typical horizontal sampling densities of 45 or 25 km are obtained, respectively. Between 6.4 and 8.7 degrees of freedom are obtained for the different target-parameters for a limb sequence with 9 limb-viewing and 2 upward-viewing observation geometries, indicating comprehensive vertical information included in the spectra.

The retrieval results are validated against available in-situ measurements carried out onboard the Geophysica during the same flight. The profile comparisons show a high degree of consistency between MIPAS-STR and the in-situ instruments, taking into account the errors of MIPAS-STR and the in-situ results, the vertical and horizontal resolution of the MIPAS-STR results, atmospheric inhomogeneities and the geograph-

AMTD
4, 7035–7108, 2011

ical and time-mismatch between the MIPAS-STR and in-situ measurements. For temperature and O_3 the results show very good agreement within the estimated errors of the involved instruments. For CFC-11 and CFC-12, higher discrepancies are apparent around flight altitude and are attributed to the observed strong contrasts in the mixing ratios of the CFCs between vortex and extra-vortex air. The comparison of the correlation of CFC-11 and CFC-12 derived from the MIPAS-STR and HAGAR measurements, respectively, overcomes the complication of limited spatial coincidence between in-situ and remote-sensing measurements and indicates enhanced agreement between the two instruments. For the in-situ comparison of H_2O, also comprehensive agreement is found.

In the retrieved vertical cross-sections of HNO_3 and CFC-11, detailed mesoscale structures are identified, which are attributed to vortex air, vortex filaments and extra-vortex air. Small-scale structures with vertical extensions down to 1 km are resolved. The vertical cross-sections of HNO_3 from MIPAS-STR and the infrared limb sounder CRISTA-NF, which were simultaneously deployed onboard the Geophysica during RECONCILE, are in very good agreement, taking into account the different characteristics of the two instruments.

The presented results give insights into the properties of the arctic UTLS in the early year 2010 and demonstrate the suitability of MIPAS-STR for quantitative studies of the chemistry and dynamics of the UTLS region with rather high spatial resolution. This allows for further studies with MIPAS-STR data on mesoscale structures, denitrification processes and chlorine activation.

Acknowledgements. We dedicate this paper to C. E. Blom, who greatly contributed to the success of MIPAS-STR onboard the M55 Geophyisca over many years. This work was supported by the EU under the grant number RECONCILE-226365-FP7-ENV-2008-1. We thank the RECONCILE coordination team, Myasishchev Design Bureau and Enviscope for making the RECONCILE field campaign a success. ECMWF data for the MIPAS-STR retrievals were obtained via NILU's NADIR database. W. Woiwode thanks A. Kleinert and G. Wetzel from IMK-ASF, Karlsruhe Institute for Technology, for helpful discussions, and M. von Hobe from IEK-7, Research Centre Jülich, as representative for the RECONCILE team for especially supporting

AMTD
4, 7035–7108, 2011

young scientists.

References

Andreae, M. O. and Crutzen, P. J.: Atmospheric Aerosols: Biogeochemical Sources and Role in Atmospheric Chemistry, Science, 276, 1052–1058, 1997.

Arnold, F. and Bührke, Th.: New H_2SO_4 and HSO_3 vapour measurements in the stratosphere – evidence for a volcanic influence, Nature, 301, 293–295, 1983.

Blom, C. E., Gulde, T., Keim, C., Kimmig, W., Piesch, C., Sartorius, C., and Fischer, H.: MIPAS-STR: Entwicklung eines Instruments für Stratosphärenflugzeuge, Statusseminar des Ozonforschungsprogramms, 1998.

Blom, C. E., Camy-Peyret, C., Catoire, V., Chance, K., Oelhaf, H., Ovarlez, J., Payan, S., Pirre, M., Piesch, C., and Wetzel, G: Validation of MIPAS temperature profiles by stratospheric balloon and aircraft measurements, Proc. ACVE-2 meeting, 3–7 May 2004, Frascati, Italy, 2004.

Boone, C. D., Walker, K. A., and Bernath, P. F.: Speed-dependent Voigt profile for water vapor in infrared remote sensing applications, J. Quant. Spectrosc. Ra., 105, 525–532, doi:10.1016/j.jqsrt.2006.11.015, 2007.

Brault, J. W.: New approach to high precision Fourier transform spectrometer design, Appl. Opt., 35, 2891–2896, 1996.

Ciurylo, R.: Shapes of pressure- and Doppler-broadened spectral lines in the core and near wings, Phys. Rev. A, 58, 1029–1039, 1998.

Coheur, P.-F., Herbin, H., Clerbaux, C., Hurtmans, D., Wespes, C., Carleer, M., Turquety, S., Rinsland, C. P., Remedios, J., Hauglustaine, D., Boone, C. D., and Bernath, P. F.: ACE-FTS observation of a young biomass burning plume: first reported measurements of C_2H_4, C_3H_6O, H_2CO and PAN by infrared occultation from space, Atmos. Chem. Phys., 7, 5437–5446, doi:10.5194/acp-7-5437-2007, 2007.

Cortesi, U., Lambert, J. C., De Clercq, C., Bianchini, G., Blumenstock, T., Bracher, A., Castelli, E., Catoire, V., Chance, K. V., De Mazière, M., Demoulin, P., Godin-Beekmann, S., Jones, N., Jucks, K., Keim, C., Kerzenmacher, T., Kuellmann, H., Kuttippurath, J., Iarlori, M., Liu, G. Y., Liu, Y., McDermid, I. S., Meijer, Y. J., Mencaraglia, F., Mikuteit, S., Oelhaf, H., Piccolo, C., Pirre, M., Raspollini, P., Ravegnani, F., Reburn, W. J., Redaelli, G., Remedios, J. J., Sembhi,

AMTD
4, 7035–7108, 2011

H., Smale, D., Steck, T., Taddei, A., Varotsos, C., Vigouroux, C., Waterfall, A., Wetzel, G., and Wood, S.: Geophysical validation of MIPAS-ENVISAT operational ozone data, Atmos. Chem. Phys., 7, 4807–4867, doi:10.5194/acp-7-4807-2007, 2007.

Curtius, J., Weigel, R., Vössing, H.-J., Wernli, H., Werner, A., Volk, C.-M., Konopka, P., Krebsbach, M., Schiller, C., Roiger, A., Schlager, H., Dreiling, V., and Borrmann, S.: Observations of meteoric material and implications for aerosol nucleation in the winter Arctic lower stratosphere derived from in situ particle measurements, Atmos. Chem. Phys., 5, 3053–3069, doi:10.5194/acp-5-3053-2005, 2005.

Dinelli, B. M., Castelli, E., Carli, B., Del Bianco, S., Gai, M., Santurri, L., Moyna, B. P., Oldfield, M., Siddans, R., Gerber, D., Reburn, W. J., Kerridge, B. J., and Keim, C.: Technical Note: Measurement of the tropical UTLS composition in presence of clouds using millimetre-wave heterodyne spectroscopy, Atmos. Chem. Phys., 9, 1191–1207, doi:10.5194/acp-9-1191-2009, 2009.

Ewen, G. B. L., Grainger, R. G., Lambert, A., and Baran, A. J.: Infrared radiative transfer modelling in a 3D scattering cloudy atmosphere: Application to limb sounding measurements of cirrus, J. Quant. Spectrosc. Ra., 96, 45–74, 2005.

Fabian, B. and Borchers, R.: Halocarbons in the stratosphere, Nature, 294, 733–735, 1981.

Fischer, H. and Oelhaf, H.: Remote Sensing of vertical profiles of atmospheric trace constitutents with MIPAS limb-emission spectrometers, Appl. Opt., 35, 2787–2796, 1996.

Fischer, H., Birk, M., Blom, C., Carli, B., Carlotti, M., von Clarmann, T., Delbouille, L., Dudhia, A., Ehhalt, D., Endemann, M., Flaud, J. M., Gessner, R., Kleinert, A., Koopman, R., Langen, J., López-Puertas, M., Mosner, P., Nett, H., Oelhaf, H., Perron, G., Remedios, J., Ridolfi, M., Stiller, G., and Zander, R.: MIPAS: an instrument for atmospheric and climate research, Atmos. Chem. Phys., 8, 2151–2188, doi:10.5194/acp-8-2151-2008, 2008.

Flaud, J.-M., Piccolo, C., and Carli, B.: A spectroscopic database for MIPAS, in: Proceedings of the ENVISAT validation workshop, ESRIN, Italy, 2002.

Flaud, J.-M., Brizzi, G., Carlotti, M., Perrin, A., and Ridolfi, M.: MIPAS database: Validation of HNO_3 line parameters using MIPAS satellite measurements, Atmos. Chem. Phys., 6, 5037–5048, doi:10.5194/acp-6-5037-2006, 2006.

Forman, M. L., Steel, W. H., and Vanasse, G.: Correction of asymmetric interferograms obtained in Fourier spectroscopy, J. Opt. Soc. Am., 56, 59–63, 1966.

Friedl-Vallon, F., Maucher, G., Seefeldner, M. Trieschmann, O., Kleinert, A., Lengel, A., Keim, C., Oelhaf, H., and Fischer, H.: Design and characterization of the ballon-borne Michelson

AMTD
4, 7035–7108, 2011

Interferometer for Passive Atmospheric Sounding (MIPAS-B2), Appl. Opt., 43, 3335–3355, 2004.
Funke, B., Stiller, G. P., von Clarmann, T., Echle, G., and Fischer, H.: CO_2 line mixing in MIPAS limb emission spectra and its influence on retrieval of atmospheric parameters, J. Quant. Spectrosc. Ra., 59, 215–230, doi:10.1016/S0022-4073(97)00121-0, 1998.
Hofmann, D. J.: Increase in the Stratospheric Background Sulfuric Acid Aerosol Mass in the Past 10 Years, Science 248, 996–1000, 1990.
Höpfner, M., Blom, C. E., von Clarmann, T., Fischer, H., Glatthor, N., Gulde, T., Hase, F., Keim, C., Kimmig, W., Lessenich, K., Piesch, C., Sartorius, C., and Stiller, G. P.: MIPAS-STR data analysis of APE-GAIA measurements, Paper presented in: IRS 2000: Current Problems in Atmospheric Radiation, edited by: Smith, W. L. and Timofeyev, Yu. M., A. Deepak Publishing, Hampton, Virginia, 1136–1139, 2000.
Höpfner, M., Blom, C. E., Echle, G., Glatthor, N., Hase, F., and Stiller, G.: Retrieval simulations for MIPAS-STR measurements, edited by: Smith, W. L., IRS 2000: Current Problems in Atmospheric Radiation; Proc. of the Internat. Radiation Symp., St. Petersburg, Russia, 24–29 July 2000 Hampton, Va., DEEPAK Publ., 2001.
Höpfner, M., Luo, B. P., Massoli, P., Cairo, F., Spang, R., Snels, M., Di Donfrancesco, G., Stiller, G., von Clarmann, T., Fischer, H., and Biermann, U.: Spectroscopic evidence for NAT, STS, and ice in MIPAS infrared limb emission measurements of polar stratospheric clouds, Atmos. Chem. Phys., 6, 1201–1219, doi:10.5194/acp-6-1201-2006, 2006.
Höpfner, M., von Clarmann, T., Fischer, H., Funke, B., Glatthor, N., Grabowski, U., Kellmann, S., Kiefer, M., Linden, A., Milz, M., Steck, T., Stiller, G. P., Bernath, P., Blom, C. E., Blumenstock, Th., Boone, C., Chance, K., Coffey, M. T., Friedl-Vallon, F., Griffith, D., Hannigan, J. W., Hase, F., Jones, N., Jucks, K. W., Keim, C., Kleinert, A., Kouker, W., Liu, G. Y., Mahieu, E., Mellqvist, J., Mikuteit, S., Notholt, J., Oelhaf, H., Piesch, C., Reddmann, T., Ruhnke, R., Schneider, M., Strandberg, A., Toon, G., Walker, K. A., Warneke, T., Wetzel, G., Wood, S., and Zander, R.: Validation of MIPAS $ClONO_2$ measurements, Atmos. Chem. Phys., 7, 257–281, doi:10.5194/acp-7-257-2007, 2007.
Junge, C. E., Chagnon, C. W., and Manson, J. E.: A World-wide Stratospheric Aerosol Layer, Science, 133, 1478–1479, 1961.
Keim, C.: Entwicklung und Verifikation der Sichtlinienstabilisierung für MIPAS auf dem hochfliegenden Forschungsflugzeug M55 Geophysica, Wissenschafltiche Berichte, FZKA 6729, Dissertation, Universität Karlsruhe, 2002.

AMTD
4, 7035–7108, 2011

Keim, C., Blom, C. E., von der Gathen, P., Gulde, T., Höpfner, M., Liu, G. Y., Oulanovsky, A., Piesch, C., Ravegnani, F., Sartorius, C., Schlager, H., and Volk, C. M.: Validation of MIPAS-ENVISAT by correlative measurements of MIPAS-STR, Proc. ACVE-2 meeting, 3–7 May 2004, Frascati, Italy, 2004.

Keim, C., Liu, G. Y., Blom, C. E., Fischer, H., Gulde, T., Höpfner, M., Piesch, C., Ravegnani, F., Roiger, A., Schlager, H., and Sitnikov, N.: Vertical profile of peroxyacetyl nitrate (PAN) from MIPAS-STR measurements over Brazil in February 2005 and its contribution to tropical UT NO_y partitioning, Atmos. Chem. Phys., 8, 4891–4902, doi:10.5194/acp-8-4891-2008, 2008.

Kimmig, W.: Das Abtastverfahren der Interferogramme des flugzeuggetragenen Fourierspektrometers MIPAS-STR, Wissenschaftliche Berichte, FZKA 6665, Dissertation, Universität Karlsruhe, 2001.

Kleinert, A.: Correction of detector nonlinearity for the balloonborne Michelson Interferometer for Passive Atmospheric Sounding, Appl. Opt., 45, 425–431, 2006.

Lengel, A.: Bestimmung der Apparatefunktion des Fourierspektrometers MIPAS-B2 aus stratosphärischen Spektren, Wissenschaftliche Berichte, FZKA 7016, Dissertation, Universität Karlsruhe, 2004.

Manuilova, R. O., Gusev, O. A., Kutepov, A. A., von Clarmann, T., Oelhaf, H., Stiller, G. P., Wegner, A., Lopez-Puertas, M., Martin-Torres, F. J., Zaragoza, G., and Flaud, J.-M.: Modelling of non-LTE limb spectra of i.r. ozone bands for the MIPAS space experiment, J. Quant. Spectrosc. Ra., 59, 405–422, doi:10.1016/S0022-4073(97)00120-9, 1998.

Moore, D. P., Waterfall, A. M., and Remedios, J. J.: The potential for radiometric retrievals of halocarbon concentrations from the MIPAS-E instrument, Adv. Space Res., 37, 2238–2246, 2006.

Murphy, D. M., Thomson, D. S., and Mahoney, M. J.: In Situ Measurements of Organics, Meteoritic Material, Mercury, and Other Elements in Aerosols at 5 to 19 Kilometers, Science, 282, 1664–1669, 1998.

Norton, H. and Beer, R.: New apodizing functions for Fourier spectrometry, J. Opt. Soc. Am., 66, 259–264, (Errata J. Opt. Soc. Am., 67, 419, 1977), 1976.

Peter, T.: Microphysics and heterogeneous chemistry of polar stratospheric clouds, Ann. Rev. Phys. Chem., 48, 785–822, 1997.

Phillips, C.: A Technique for the Numerical Solution of Certain Integral Equations of the First Kind, J. Assoc. Comput. Math., 9, 84–97, 2003.

Piesch, C., Gulde, T., Sartorius, C., Friedl-Vallon, F., Seefeldner, M., Wölfel, M., Blom, C. E.,

AMTD
4, 7035–7108, 2011

and Fischer, H.: Design of a MIPAS instrument for high-altitude aircraft, Proc. of the 2nd Internat. Airborne Remote Sensing Conference and Exhibition, ERIM, Ann Arbor, MI, Vol. II, 199–208, 1996.

Purser, R. J. and Huang, H.-L.: Estimating effective data density in a satellite retrieval or an objective analysis, J. Appl. Meteorol., 32, 1092–1107, 1993.

Razavi, A., Karagulian, F., Clarisse, L., Hurtmans, D., Coheur, P. F., Clerbaux, C., Müller, J. F., and Stavrakou, T.: Global distributions of methanol and formic acid retrieved for the first time from the IASI/MetOp thermal infrared sounder, Atmos. Chem. Phys., 11, 857–872, doi:10.5194/acp-11-857-2011, 2011.

Remedios, J. J., Leigh, R. J., Waterfall, A. M., Moore, D. P., Sembhi, H., Parkes, I., Greenhough, J., Chipperfield, M.P., and Hauglustaine, D.: MIPAS reference atmospheres and comparisons to V4.61/V4.62 MIPAS level 2 geophysical data sets, Atmos. Chem. Phys. Discuss., 7, 9973–10017, doi:10.5194/acpd-7-9973-2007, 2007.

Riediger, O., Volk, C. M., Strunk, M., and Schmidt, U.: HAGAR – A new in situ tracer instrument for stratospheric balloons and high altitude aircraft, Eur. Comm. Air Pollut. Res. Report, 73, 727–730, 2000.

Rodgers, C. D.: Inverse Methods for Atmospheric Sounding: Theory and Practice, Vol. 2 of Series on Atmospheric, Oceanic and Planetary Physics, edited by: Taylor, F. W., World Scientific, 2000.

Schneider, M., Hase, F., Blavier, J.-F., Toon, G.C., and Leblanc, T.: An empirical study on the importance of a speed-dependent Voigt line shape model for tropospheric water vapor profile remote sensing, J. Quant. Spectrosc. Ra., 112, 465–474, doi:10.1016/j.jqsrt.2010.09.008, 2011.

Shur, G. N., Yushkov, V. A., Drynkov, A. V., Fadeeva, G. V., and Potertikova, G. A.: Study of Thermodynamics of the Stratosphere at High Latitudes of the Northern Hemisphere on the M-55 Geofizika Flying Laboratory, Russ. Meteorol. Hydrol., 8, 43–53, 2006.

Sitnikov, N. M., Yushkov, V. A., Afchine, A. A., Korshunov, L. I., Astakhov, V. I., Ulanovskii, A. E., Krämer, M., Mangold, A., Schiller, C., and Ravegnani, F.: The FLASH instrument for water vapor measurements on board the high-altitude airplane, Instrum. Exp. Tech., 50, 113–121, doi:10.1134/S0020441207010174, 2007.

Smith, W. L., Ackerman, S., Revercomb, H., Huang, H., DeSlover, D. H., Feltz, W., Gumley, L., and Collard, A.: Infrared spectral absorption of nearly invisible cirrus clouds, Geophys. Res. Lett., 25, 1137–1140, doi:10.1029/97GL03491, 1998.

AMTD
4, 7035–7108, 2011

Spang, R., Eidmann, G., Riese, M., Offermann, D., Preusse, P., Pfister, L., and Wang, P.-H.: CRISTA observations of cirrus clouds around the tropopause, J. Geophys. Res., 107, 8174, doi:10.1029/2001JD000698, 2002.

Spang, R., Remedios, J. J., and Barkley, M. P.: Colour indices for the detection and differentiation of cloud types in infra-red limb emission spectra, Adv. Space Res., 33, 1041–1047, 2004.

Spang, R., Remedios, J. J., Kramer, L. J., Poole, L. R., Fromm, M. D., Müller, M., Baumgarten, G., and Konopka, P.: Polar stratospheric cloud observations by MIPAS on ENVISAT: detection method, validation and analysis of the northern hemisphere winter 2002/2003, Atmos. Chem. Phys., 5, 679–692, doi:10.5194/acp-5-679-2005, 2005.

Spang, R., Hoffmann, L., Kullmann, A., Olschewski, F., Preusse, P., Knieling, P., Schroeder, S., Stroh, F., Weigel, K., and Riese, M.: High resolution limb observations of clouds by the CRISTA-NF experiment during the SCOUT-O_3 tropical aircraft campaign, J. Adv. Space, Res., 42, 1765–1775, doi:10.1016/j.asr.2007.09.036, 2008.

Steck, T.: Methods for determining regularization for atmospheric retrieval problems, Appl. Opt., 41, 1788–1797, 2002.

Stiller, G. P. (Ed.) with contributions from von Clarmann, T., Dudhia, A., Echle, G., Funke, B., Glatthor, N., Hase, F., Höpfner, M., Kellmann, S., Kemnitzer, H., Kuntz, M., Linden, A., Linder, M., Stiller, G. P., and Zorn, S.: The Karlsruhe Optimized and Precise Radiative Transfer Algorithm (KOPRA), Wissenschaftliche Berichte, FZKA 6487, Forschungszentrum Karlsruhe, 2000.

Stiller, G. P., von Clarmann, T., Funke, B., Glatthor, N., Hase, F., Höpfner, and M., Linden, A.: Sensitivity of trace gas abundances retrievals from infrared limb emission spectra to simplifying approximations in radiative transfer modelling, J. Quant. Spectrosc. Ra., 72, 249–280, doi:10.1016/S0022-4073(01)00123-6, 2002.

Tikhonov, A.: On the Solution of Incorrectly Stated Problems and a Method of Regularisation, Dokl. Acad. Nauk SSSR, 151, 501–504, 1963.

Trieschmann, O., Friedl-Vallon, F., Lengel, A., Oelhaf, H., Wetzel, G., and Fischer H.: An advanced phase correction approach to obtain radiometric calibrated spectra of the optically well balanced balloon borne Fourier Transform Spectrometer MIPAS-B2, Optical Spectroscopic Techniques and Instrumentation for Atmospheric and Space Research III, edited by: Larar, A. M., SPIE, 3756, 17–24, 1999.

Ulanovsky, A. E., Yushkov, V. A., Sitnikov, N. M., and Ravegnani, F.: The FOZAN-II Fast-

AMTD
4, 7035–7108, 2011

Response Chemiluminescent Airborne Ozone Analyzer, Instrum. Exp. Tech., 44, 249–256, 2001.

Ungermann, J., Kalicinsky, C., Olschewski, F., Knieling, P., Hoffmann, L., Blank, J., Woiwode, W., Oelhaf, H., Hösen, E., Volk, C. M., Ulanovsky, A., Ravegnani, F., Weigel, K., Stroh, F., and Riese, M.: CRISTA-NF measurements with unprecedented vertical resolution during the RECONCILE aircraft campaign, Atmos. Meas. Tech. Discuss., submitted, 2011.

von Clarmann, T.: Zur Fernerkundung der Erdatmosphäre mittels Infrarotspektroskopie: Rekonstruktionstheorie und Anwendung, Wissenschaftliche Berichte, FZKA 6928, Forschungszentrum Karlsruhe, 2003.

Wagner, G. and Birk, M.: New infrared spectroscopic database for chlorine nitrate, J. Quant. Spectrosc. Ra., 82, 443–460, 2003.

Wang, D. Y., Höpfner, M., Blom, C. E., Ward, W. E., Fischer, H., Blumenstock, T., Hase, F., Keim, C., Liu, G. Y., Mikuteit, S., Oelhaf, H., Wetzel, G., Cortesi, U., Mencaraglia, F., Bianchini, G., Redaelli, G., Pirre, M., Catoire, V., Huret, N., Vigouroux, C., De Mazière, M., Mahieu, E., Demoulin, P., Wood, S., Smale, D., Jones, N., Nakajima, H., Sugita, T., Urban, J., Murtagh, D., Boone, C. D., Bernath, P. F., Walker, K. A., Kuttippurath, J., Kleinböhl, A., Toon, G., and Piccolo, C.: Validation of MIPAS HNO_3 operational data, Atmos. Chem. Phys., 7, 4905–4934, doi:10.5194/acp-7-4905-2007, 2007.

Werner, A., Volk, C. M., Ivanova, E. V., Wetter, T., Schiller, C., Schlager, H., and Konopka, P.: Quantifying transport into the Arctic lowermost stratosphere, Atmos. Chem. Phys., 10, 11623–11639, doi:10.5194/acp-10-11623-2010, 2010.

Wetzel, G., Oelhaf, H., Ruhnke, R., Friedl-Vallon, F., Kleinert, A., Kouker, W., Maucher, G., Reddmann, T., Seefeldner, M., Stowasser, M., Trieschmann, O., von Clarmann, T., and Fischer, H.: NO_y partitioning and budget and its correlation with N_2O in the Arctic vortex and in summer midlatitudes in 1997, J. Geophys. Res., 107, 4280, doi:10.1029/2001JD000916, 2002.

AMTD
4, 7035–7108, 2011

Table 1. Characteristics of MIPAS-STR in the current configuration.

Telescope	
Field of view (full cone)	0.44°
Etendue	2.6×10^{-3} sr cm^2
Interferometer	
Effective optical path difference	±13.9 cm
Scan time per interferogram	~9.5 sec
Sampling frequency	48.8 kHz
Signal frequency	2.1–6.1 kHz
Unapodized/apodized spectral resolution	0.036 cm^{-1}/0.058 cm^{-1}
Detectors	Si:As – BIB
NESR (single apodized spectrum, in-flight)	
Channel 1 (725–990 cm^{-1})	1×10^{-8} W/(cm^2 sr cm^{-1})
Channel 2 (1150–1360 cm^{-1})	8×10^{-9} W/(cm^2 sr cm^{-1})
Channel 3 (1560–1710 cm^{-1})	5×10^{-9} W/(cm^2 sr cm^{-1})
Channel 4 (1810–2100 cm^{-1})	5×10^{-9} W/(cm^2 sr cm^{-1})
Pointing	
Pitch/roll accuracy (AHRS)	0.5 arcmin (1σ)
Yaw accuracy (AHRS)	0.3° (1σ)
Estimated LOS-elevation accuracy	0.78 arcmin (1σ)
Dimensions	
Optics module	135 × 75 × 75 cm^3
Electronics module	50 × 50 × 50 cm^3
Total mass	~200 kg
Power consumption	~300 W (28 V DC)

AMTD
4, 7035–7108, 2011

Table 2. Microwindows and target signatures selected for the retrievals. Spectral positions of the most prominent target signatures are listed. For cross-section gases, the spectral signatures are relevant in the whole range of the microwindow.

Retrieval target	Microwindow [cm^{-1}]	Target signature	Spectral position [cm^{-1}]
LOS/temperature (CO_2 signatures)	810.1–813.1	R24e (11101←10002) R26e (11101←10002)	810.93 812.48
	955.6–958.5	P6e (00011←10001) P4e (00011←10001)	956.19 957.80
HNO_3	866.0–870.0	$\nu5/2\nu9$ bands	9 prominent lines ($\nu5$-band)
O_3	780.6–781.7	$\nu2$-band	780.80 781.13 781.18 781.52
	787.0–788.0	$\nu2$-band	787.13 787.46 787.86
CFC-11	842.5–848.0	$\nu4$-band	cross-section
CFC-12	918.9–920.6 921.0–922.8	$\nu6$-band $\nu6$-band	cross-section cross-section
$ClONO_2$	779.8–780.5 805.1–805.5	$\nu4$-band $\nu3$-band	cross-section cross-section
H_2O	795.7–796.1	pure rotation	795.89

AMTD
4, 7035–7108, 2011

Table 3. In-situ instruments onboard the Geophysica used for comparisions with MIPAS-STR.

Instrument	Target	Time resolution	Accuracy	Reference
TDC	Temperature	1 s	0.5 K	Shur et al. (2007)
FOZAN	O_3	2 s	< 10 %	Ulanovsky et al. (2001)
HAGAR	CFC-11	90 s	0.5–5 ppt (1.4–5.6 %)	Riediger et al. (2000) Werner et al. (2010)
HAGAR	CFC-12	90 s	2–8 ppt (1.2–1.7 %)	Riediger et al. (2000) Werner et al. (2010)
FLASH-A	H_2O (gas)	4 s	10 %	see text

AMTD
4, 7035–7108, 2011

Table 4. Mean differences and sample standard deviations (1σ, in parentheses) of the mean differences between MIPAS-STR and in-situ results for profile comparison and comparison along flight track.

Target	Vertical profile		Flight track	
Temperature	0.21 (0.73) K		−0.19 (0.64) K	
O_3	−0.01 (0.12) ppmv	−3 (14) %	0.05 (0.26) ppmv	2 (9) %
CFC-11	17 (9) pptv	14 (13) %	8 (24) pptv	21 (40) %
CFC-12	21(19) pptv	5 (5) %	14 (42) pptv	8 (16) %
H_2O	1.16 (1.91) ppmv	8 (14) %	0.29 (0.36) ppmv	6 (7) %

AMTD
4, 7035–7108, 2011

Table 5. Characteristics of CRISTA-NF. The spectral resolution is given for the low resolution spectrometer (LRS) which is capable of the detection of HNO_3.

CRISTA-NF	
Spectrometer type	2 Ebert-Fastie Grating Spectrometers
Spectral range	667–2500 cm^{-1}
Spectral resolution	1.6 cm^{-1} (LRS)
FOV (vertical x horizontal)	3 × 300 arcmin
Vertical/horizontal sampling density	0.25/15 km
Time per spectrum/limb scan	~1.2/70 sec

AMTD
4, 7035–7108, 2011

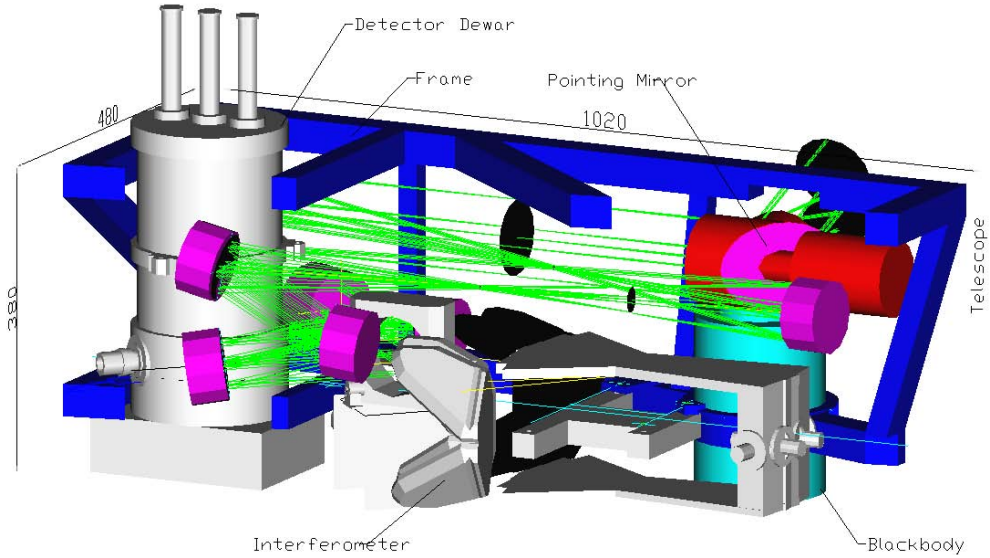

Fig. 1. Schematic representation of the optics module of MIPAS-STR (taken from Blom et al., 1998). Mirrors are shown in pink and the light path along scan-mirror, telescope and interferometer towards the detector dewar is indicated by green lines.

AMTD
4, 7035–7108, 2011

MIPAS-STR measurements in the arctic UTLS in winter/spring 2010

W. Woiwode et al.

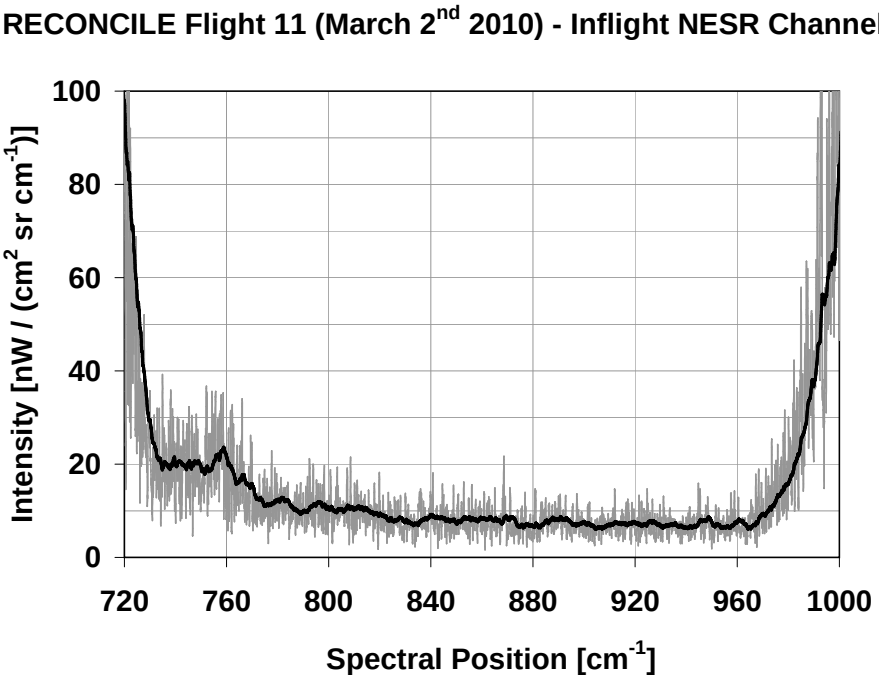

Fig. 2. Typical NESR of a single channel 1 spectrum under flight conditions (grey curve) and moving average (black curve).

AMTD
4, 7035–7108, 2011

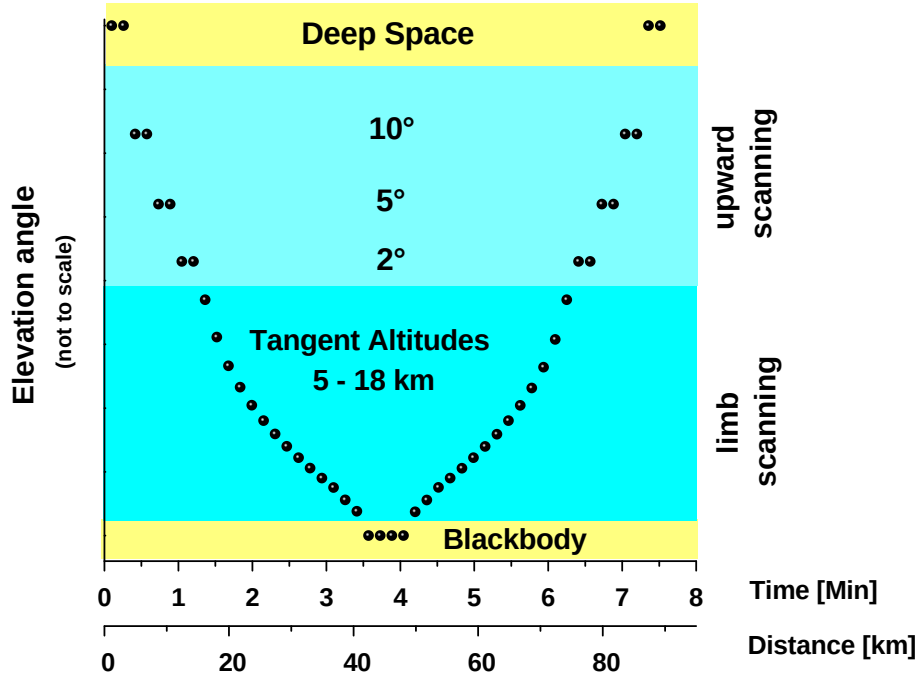

Fig. 3. Schematic representation of the standard sampling programme of MIPAS-STR, including atmospheric measurements (cyan) and calibration measurements (yellow). Two full limb scans are shown.

AMTD
4, 7035–7108, 2011

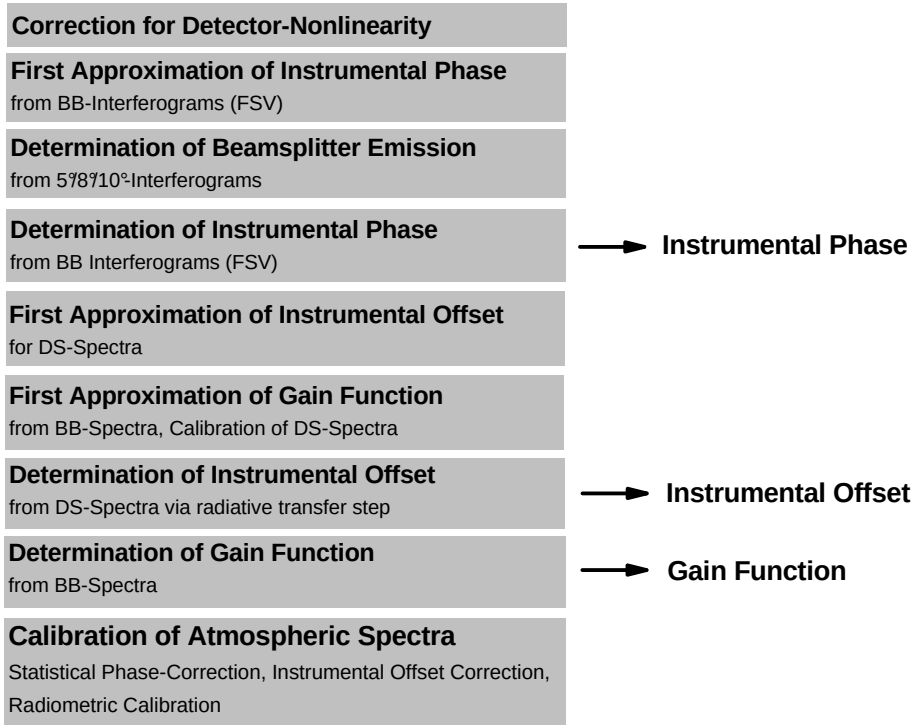

Fig. 4. Schematic representation of the full calibration cycle for MIPAS-STR measurements, including the determination of the detector non-linearity, instrumental phase, instrumental offset and radiometric gain function (BB = blackbody measurements, DS = "deep space" measurements (zenith view), FSV = phase correction according to Forman, Steel and Vanasse, for details see text).

AMTD
4, 7035–7108, 2011

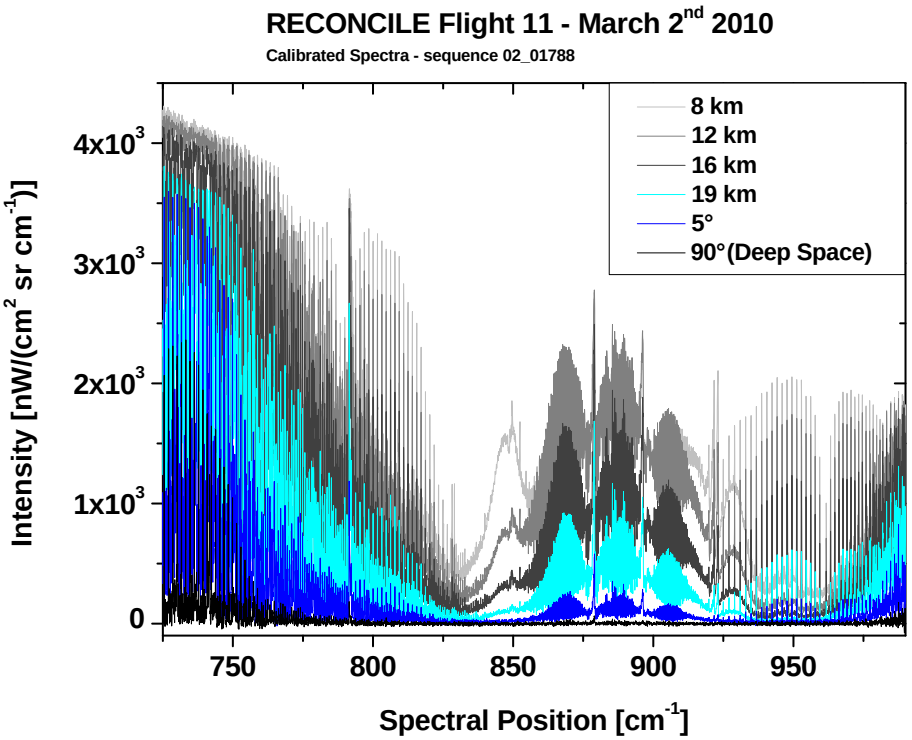

Fig. 5. Examples for single calibrated spectra from RECONICLE flight 11 on 2 March 2010. In the box in the upper right side, the corresponding tangent altitudes/elevation angles of the spectra are listed (0° elevation corresponds to horizontal view).

AMTD
4, 7035–7108, 2011

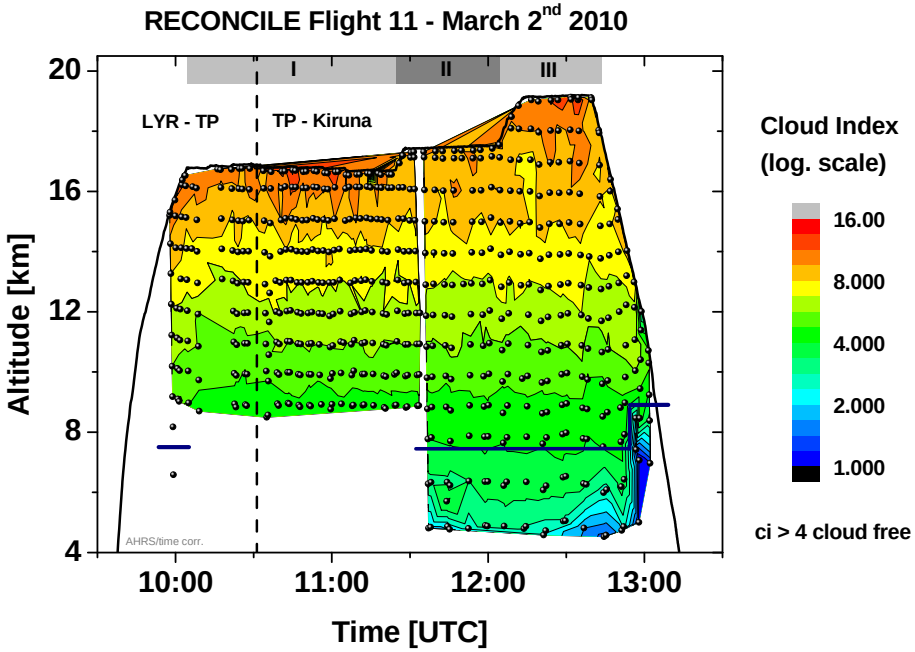

Fig. 6. Vertical distribution of tangent points (points) and interpolated cloud index (ci, contour). Flight altitude of the Geophysica (solid black line) along flight track from Longyearbyen (LYR) via the turning point (TP, dashed black line) to Kiruna. The horizontal blue lines represent the approximate threshold for cloud index 4.

AMTD
4, 7035–7108, 2011

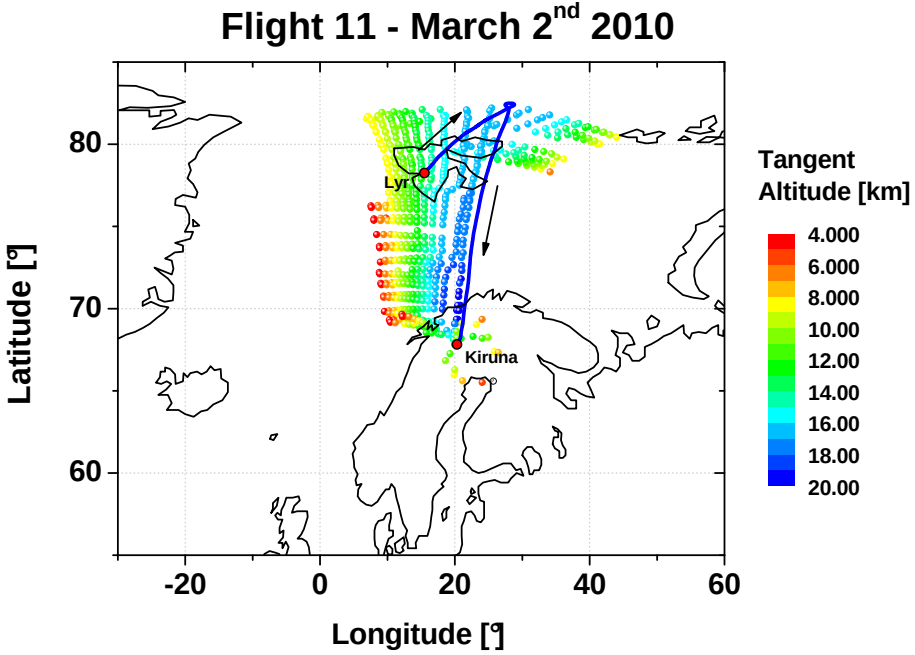

Fig. 7. Flight track of the Geophyscia for RECONCILE flight 11 (solid blue line) and distribution of tangent points of the MIPAS-STR observations, colour-coded with reference to the tangent altitude.

AMTD
4, 7035–7108, 2011

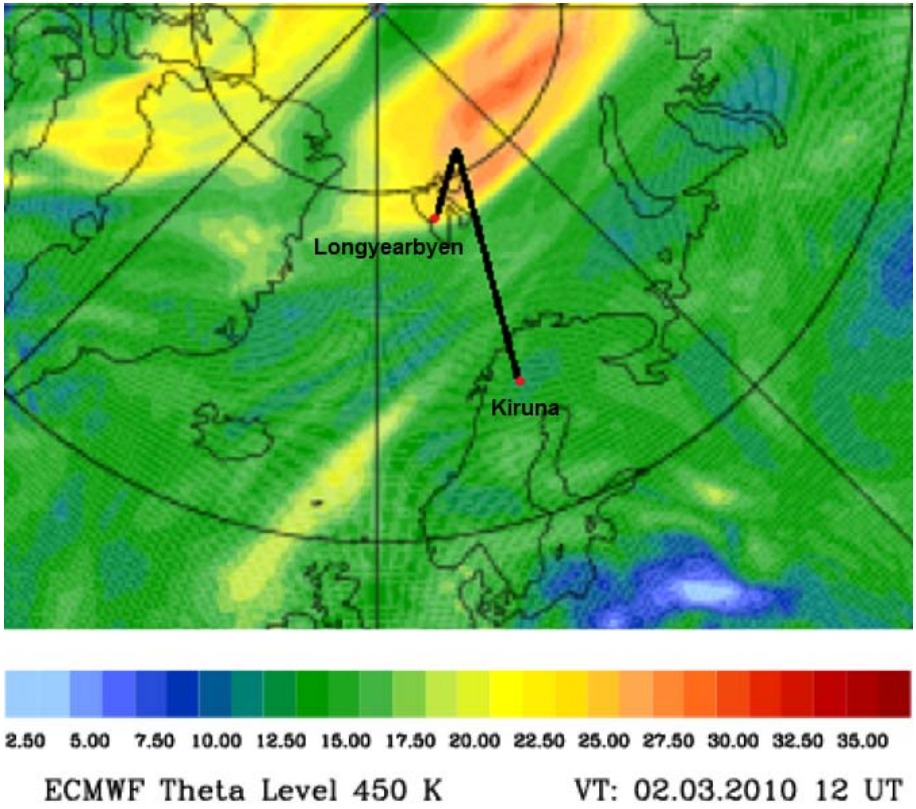

Fig. 8. Meteorological situation during RECONCILE Flight 11. The colour-coding of the map shows the potential vorticity at the 450 K-level (approximately 17 km altitude). A late vortex remnant, coming from Canada and reaching from Spitsbergen to Siberia, can be identified clearly. The flight path of the Geophysica is indicated schematically.

AMTD
4, 7035–7108, 2011

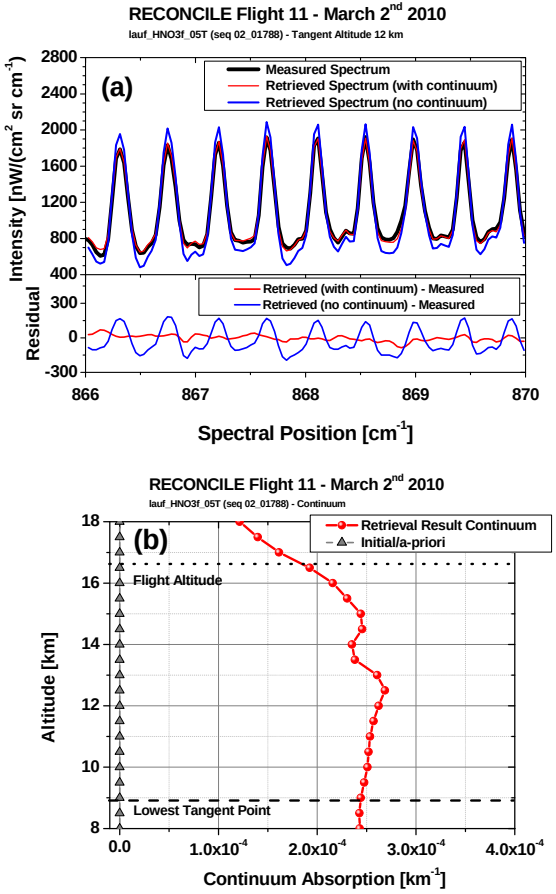

Fig. 9. **(a)** Measured spectrum (black) and retrieved spectra with (red) and without (blue) background continuum retrieval for a flight altitude of 16.7 km and a tangent altitude of 12 km for the HNO_3-retrieval and residuals. **(b)** Associated retrieval result for continuum absorption of the corresponding full limb sequence.

AMTD
4, 7035–7108, 2011

MIPAS-STR measurements in the arctic UTLS in winter/spring 2010

W. Woiwode et al.

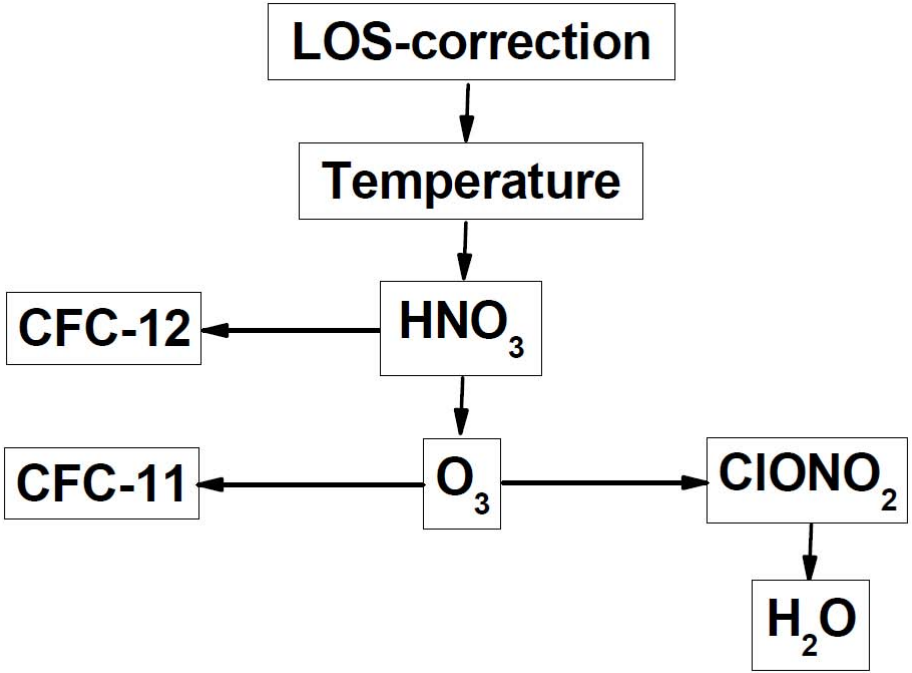

Fig. 10. Schematic representation of the subsequent retrievals of LOS correction, temperature and the discussed trace gases from MIPAS-STR channel 1 spectra. For each target parameter, all other parameters prior in the scheme are determined previously.

AMTD
4, 7035–7108, 2011

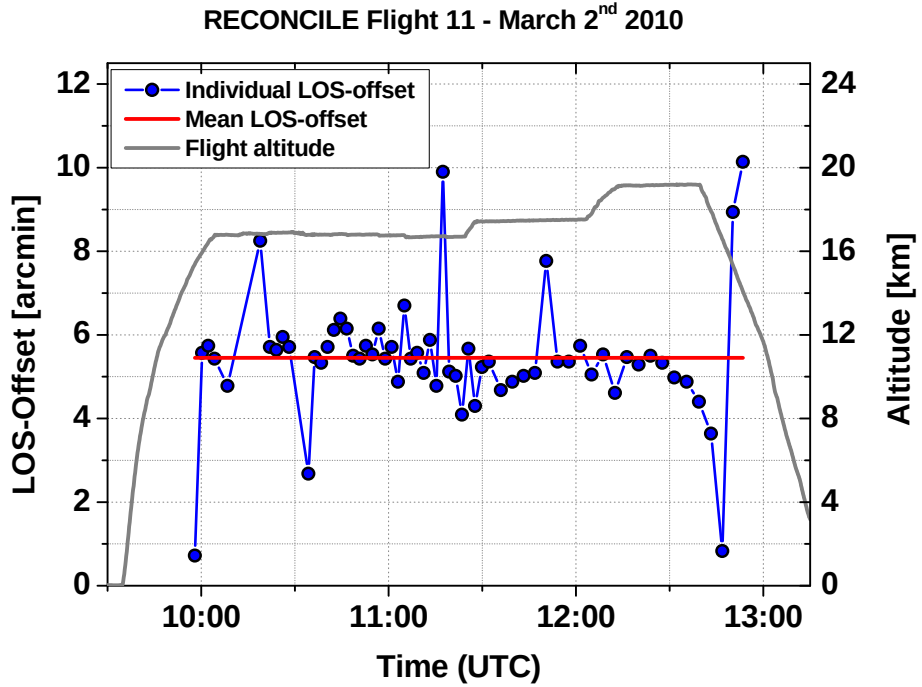

Fig. 11. Retrieved LOS offsets from the individual limb sequences and mean LOS offset used as LOS correction.

AMTD
4, 7035–7108, 2011

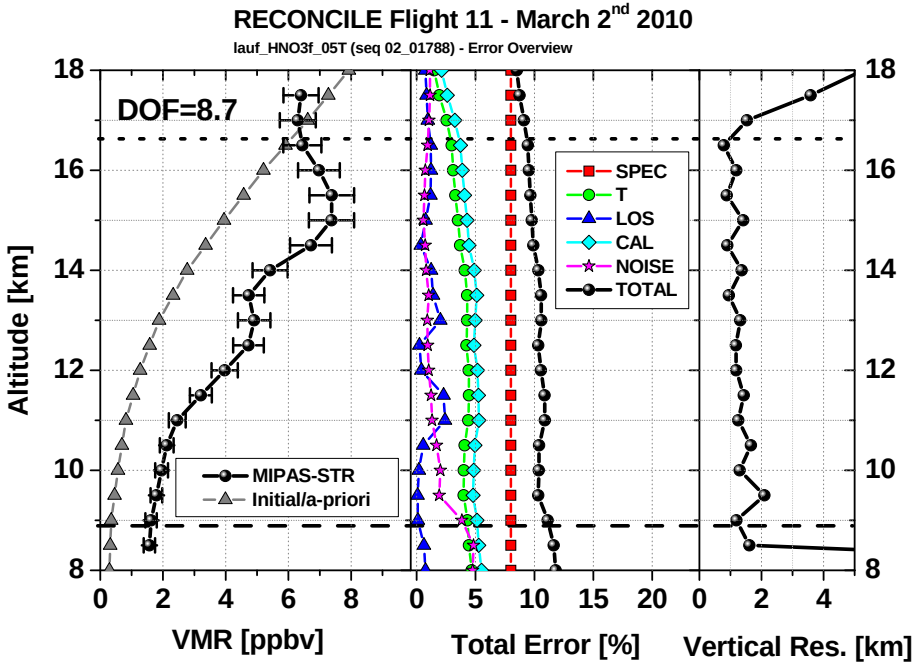

Fig. 12. Left side: retrieved vertical profile of HNO_3 with estimated error and initial guess/a priori profile (DOF = degrees of freedom). Middle: Different error contributions and estimated error in percent (SPEC = spectroscopic data, T = temperature, LOS = line-of-sight, CAL = radiometric calibration, NOISE = spectral noise, TOTAL = estimated 1σ-error). Right side: Vertical resolution of the retrieval result. The dotted horizontal line indicates the flight altitude of the Geophyisca and the dashed horizontal line the lowest tangent point of the scan.

AMTD
4, 7035–7108, 2011

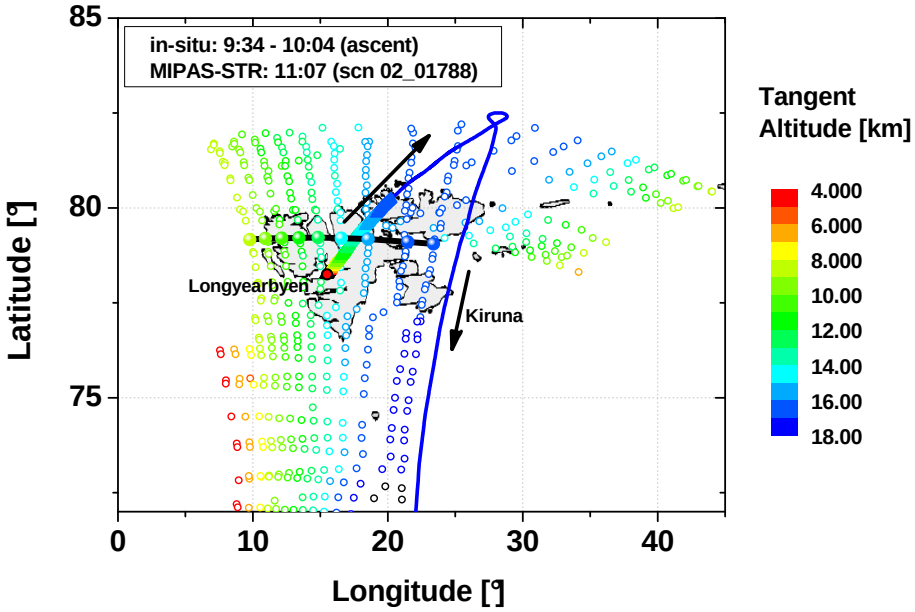

Fig. 13. Limb scan of MIPAS-STR selected for comparisons with in-situ profiles. The distribution of the tangent points of MIPAS-STR (circles) along the flight path (blue line) is indicated colour-coded with reference to the tangent altitude. The selected scan 02_01788 for the comparisons is indicated by filled circles. The flight altitude of the Geophysica is plotted colour-coded with altitude for the ascent phase.

AMTD
4, 7035–7108, 2011

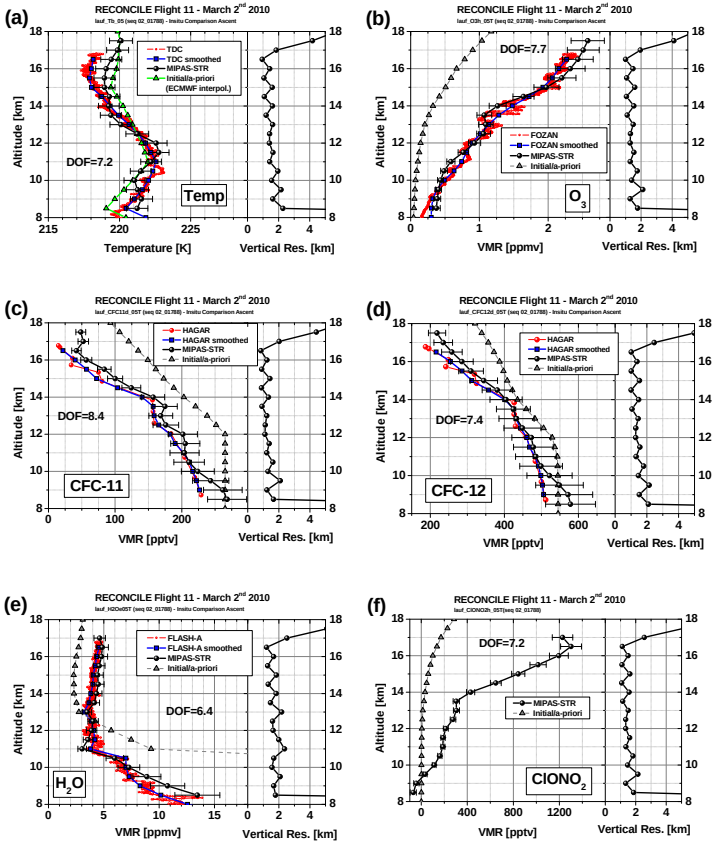

Fig. 14. (a–f): Retrieved profiles of temperature, O_3, CFC-11, CFC-12, H_2O and $ClONO_2$ with estimated error and comparison with in-situ measurements (left panels in the plots). Initial-guess/a priori profiles for the retrievals and DOF of the results are also indicated. Vertical resolutions of the retrieval results (right panels in the plots).

AMTD
4, 7035–7108, 2011

MIPAS-STR measurements in the arctic UTLS in winter/spring 2010

W. Woiwode et al.

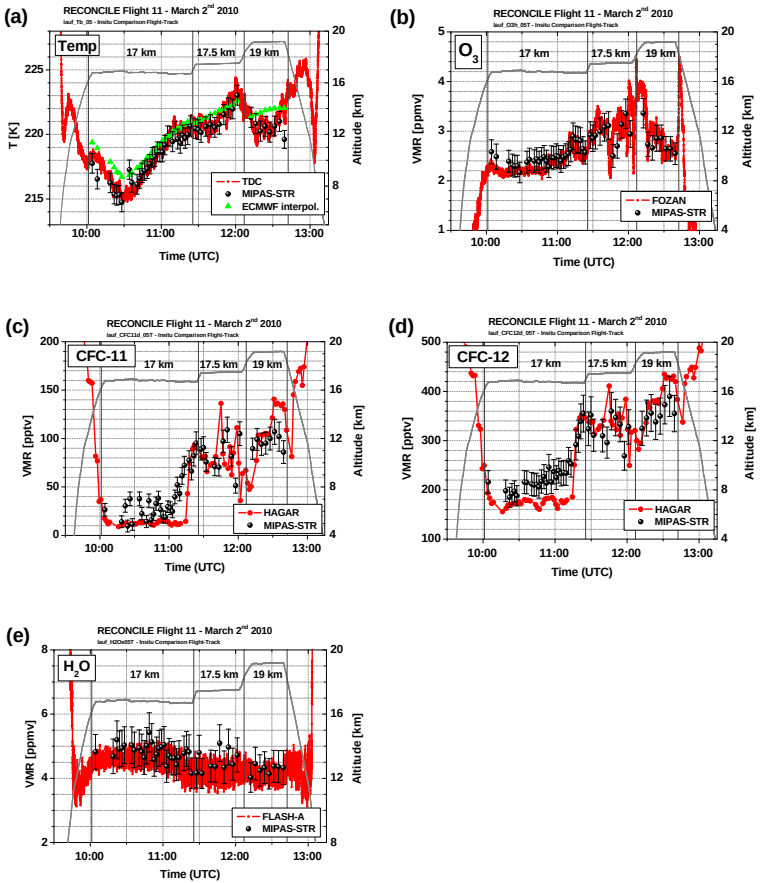

Fig. 15. (a–e): Comparison of the retrieval results inclusive estimated error for temperature, O_3, CFC-11, CFC-12 and H_2O with in-situ measurements along flight track. Retrieval results are shown for the indicated retrieval-grid altitudes.

AMTD
4, 7035–7108, 2011

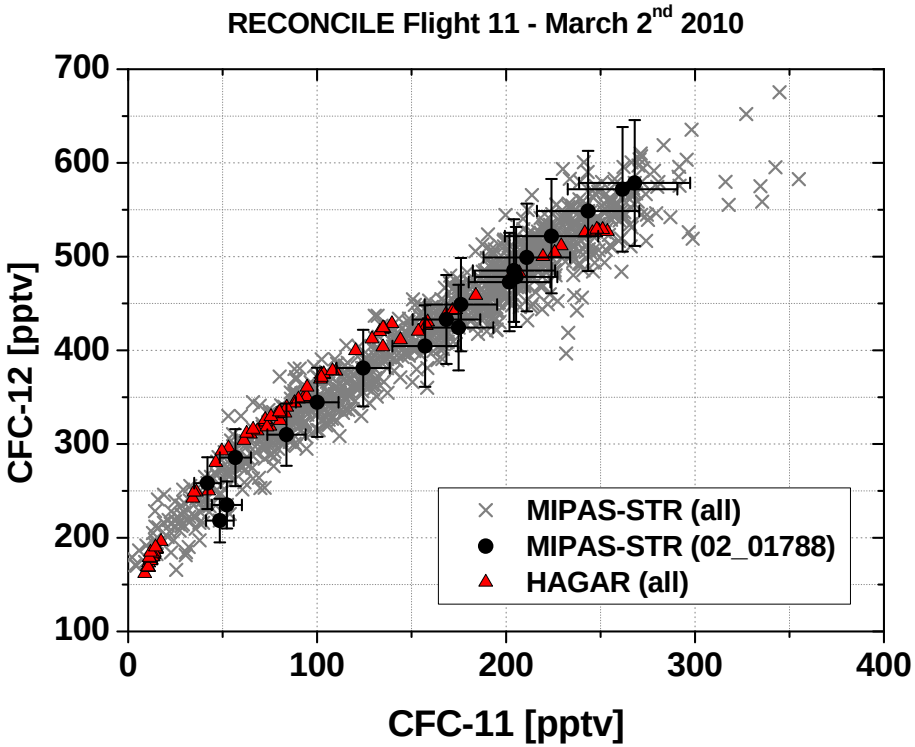

Fig. 16. Correlation of CFC-11 and CFC-12 derived from the MIPAS-STR and HAGAR measurements for RECONCILE flight 11. For MIPAS-STR, all retrieved profile points with a vertical resolution better than 5 km are shown. The points associated to sequence 02_01788 of MIPAS-STR, for which the in-situ profile-comparisons are carried out, are shown together with the corresponding estimated 1σ-errors.

AMTD
4, 7035–7108, 2011

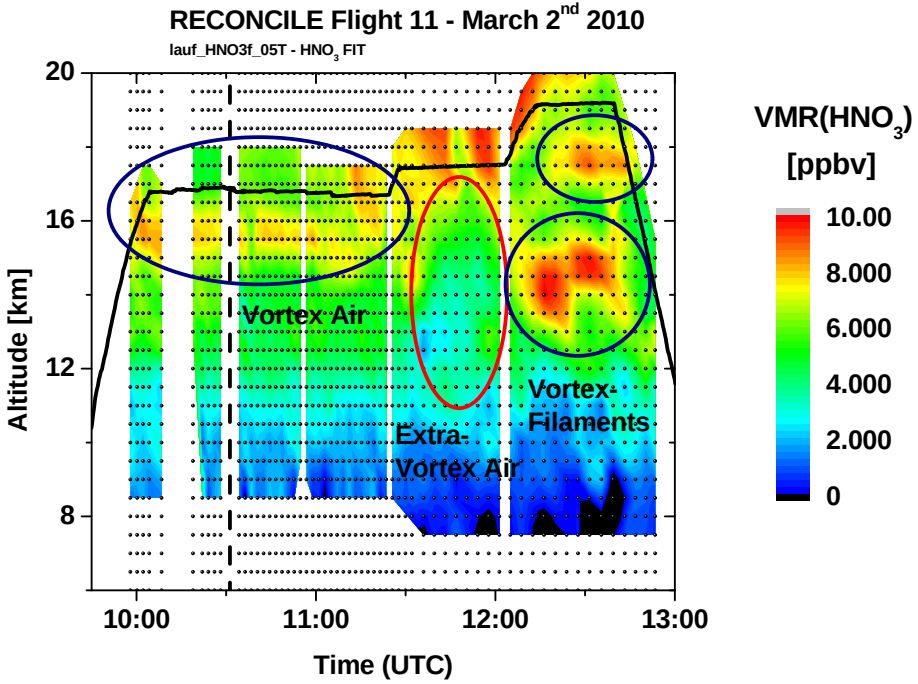

Fig. 17. Vertical cross-section of HNO_3 along flight track derived from MIPAS-STR measurements. The turn between the north-eastern flight leg (from Longyearbyen) to the southward flight leg (towards Kiruna) is indicated by the dashed vertical line. Retrieved HNO_3-mixing ratios are linearly interpolated between the retrieval grid points (black dots) and are shown colour-coded. Interpolation is performed between grid points with vertical resolutions of the result of better than 5 km.

AMTD
4, 7035–7108, 2011

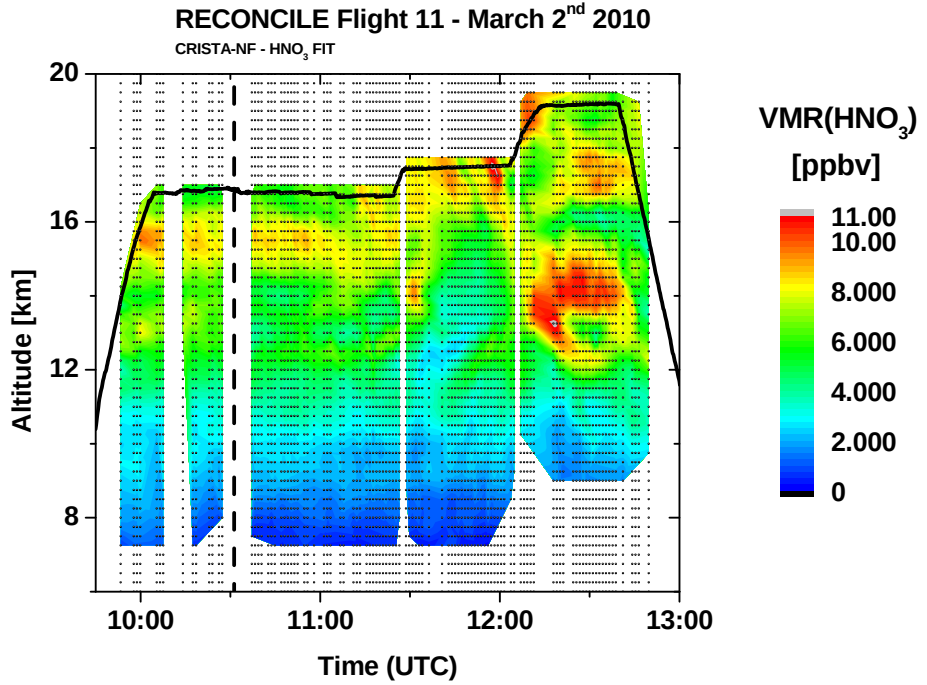

Fig. 18. Vertical cross-section of HNO_3 along flight track derived from CRISTA-NF measurements (compare Fig. 17).

AMTD
4, 7035–7108, 2011

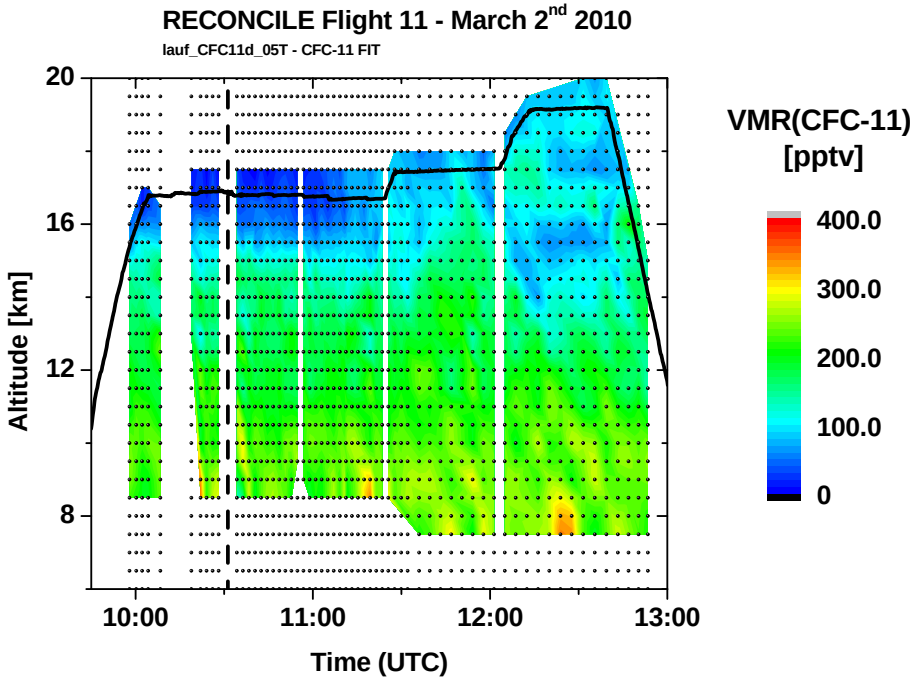

Fig. 19. Vertical cross-section of CFC-11 along flight track derived from MIPAS-STR measurements (compare Fig. 17).

AMTD
4, 7035–7108, 2011